nature microbiology

Article

https://doi.org/10.1038/s41564-024-01784-w

# The adhesin RadD enhances *Fusobacterium nucleatum* tumour colonization and colorectal carcinogenesis

Received: 22 November 2023

Accepted: 15 July 2024

Published online: 21 August 2024

Check for updates

Lu Zhang[1,6], Xiao-Xu Leng[1,6], Jianxun Qi[2], Ni Wang[1], Ji-Xuan Han[1], Zhi-Hang Tao[1], Zi-Yan Zhuang[1], Yimeng Ren[1], Yi-Le Xie[1], Shan-Shan Jiang[1], Jia-Lu Li[1], Huimin Chen[1], Cheng-Bei Zhou[1], Yun Cui[1], Xiaoyu Chen[1], Zheng Wang[3], Zi-Zhen Zhang[3], Jie Hong[1], Hao-Yan Chen[1], Weihong Jiang[4], Ying-Xuan Chen[1], Xin Zhao[2], Jun Yu[5] & Jing-Yuan Fang[1]

*Fusobacterium nucleatum* can bind to host cells and potentiate intestinal tumorigenesis. Here we used a genome-wide screen to identify an adhesin, RadD, which facilitates the attachment of *F. nucleatum* to colorectal cancer (CRC) cells in vitro. RadD directly binds to CD147, a receptor overexpressed on CRC cell surfaces, which initiated a PI3K–AKT–NF–κB–MMP9 cascade, subsequently enhancing tumorigenesis in mice. Clinical specimen analysis showed that elevated *radD* gene levels in CRC tissues correlated positively with activated oncogenic signalling and poor patient outcomes. Finally, blockade of the interaction between RadD and CD147 in mice effectively impaired *F. nucleatum* attachment and attenuated *F. nucleatum*-induced oncogenic response. Together, our study provides insights into an oncogenic mechanism driven by *F. nucleatum* RadD and suggests that the RadD–CD147 interaction could be a potential therapeutic target for CRC.

Colorectal cancer (CRC) ranks third globally among cancers and is the second leading cause of cancer-related death[1,2]. A distinctive feature of CRC is its close association with the gut microbiota, which constitutes a critical component of the tumour microenvironment. Over the past decade, several 'driver' bacteria, such as polyketide synthase positive *Escherichia coli* (*pks*$^+$ *E. coli*)[3], enterotoxigenic *Bacteroides fragilis*[4] and *Peptostreptococcus anaerobius*[5] have been identified in association with the development of CRC. These pathogenic microorganisms release toxins to induce DNA damage or directly attach to cancer cells to activate oncogenic signalling cascades, thereby actively contributing to tumorigenesis[6–8].

Recently, large-scale clinical metagenomic studies have revealed that *Fusobacterium nucleatum* is notably abundant in human CRCs and adenomas[9–16], and increased levels of *F. nucleatum* correlate positively with the degree of tumour progression and high recurrence rate[17–20]. One of the key virulence characteristics of *F. nucleatum* is its capacity to bind to receptors expressed on host cells, thereby stimulating cancer cell proliferation or inhibiting immune function, leading to the initiation and advancement of CRC. For example, *F. nucleatum* expresses an adhesin FadA, of which binding to E-cadherin on colonic epithelial cells instigates the Wnt/β-catenin signalling pathway associated with carcinogenesis[21–26]. Another cell-surface adhesin, Fap2, binds

[1]Division of Gastroenterology and Hepatology, Shanghai Institute of Digestive Disease, NHC Key Laboratory of Digestive Diseases, State Key Laboratory of Systems Medicine for Cancer, Renji Hospital, School of Medicine, Shanghai Jiao Tong University, Shanghai, China. [2]CAS Key Laboratory of Pathogen Microbiology and Immunology, Institute of Microbiology, Chinese Academy of Sciences, Beijing, China. [3]Department of Gastrointestinal Surgery, Renji Hospital, School of Medicine, Shanghai Jiao Tong University, Shanghai, China. [4]CAS-Key Laboratory of Synthetic Biology, CAS Center for Excellence in Molecular Plant Sciences, Shanghai Institute of Plant Physiology and Ecology, Chinese Academy of Sciences, Shanghai, China. [5]Institute of Digestive Disease and Department of Medicine and Therapeutics, The Chinese University of Hong Kong, Hong Kong SAR, China. [6]These authors contributed equally: Lu Zhang, Xiao-Xu Leng. e-mail: jingyuanfang@sjtu.edu.cn

https://doi.org/10.1038/s41564-024-01784-w

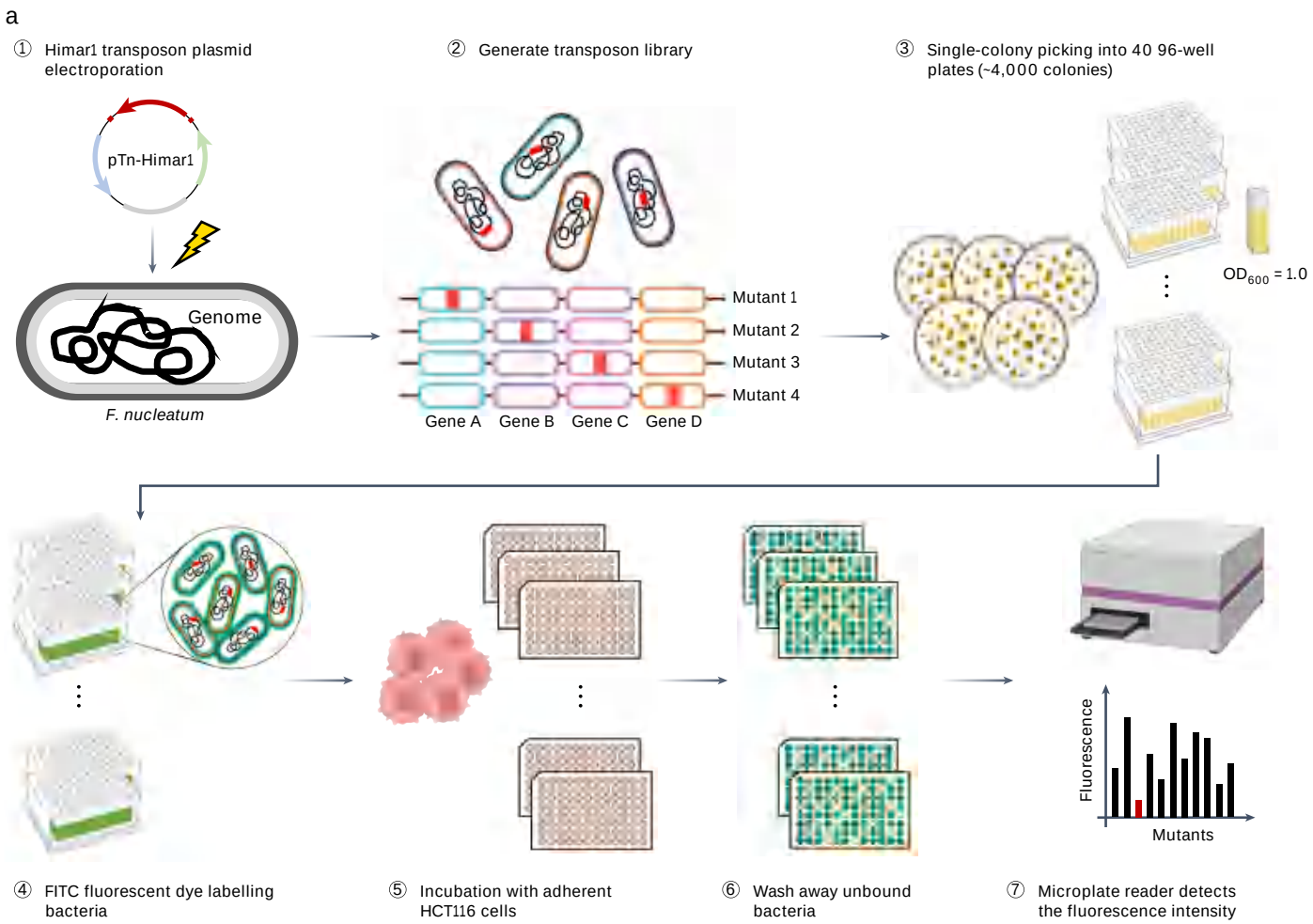


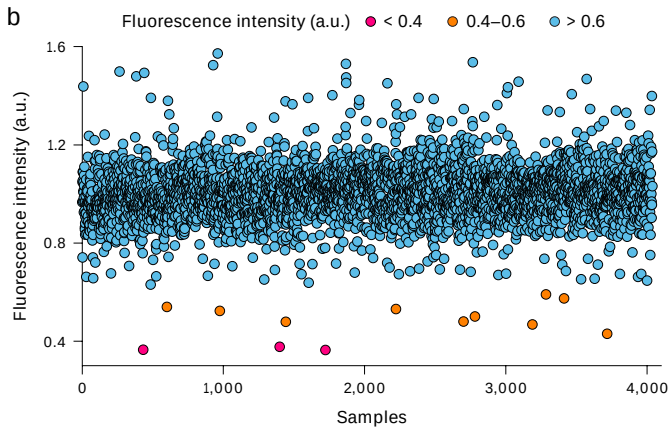


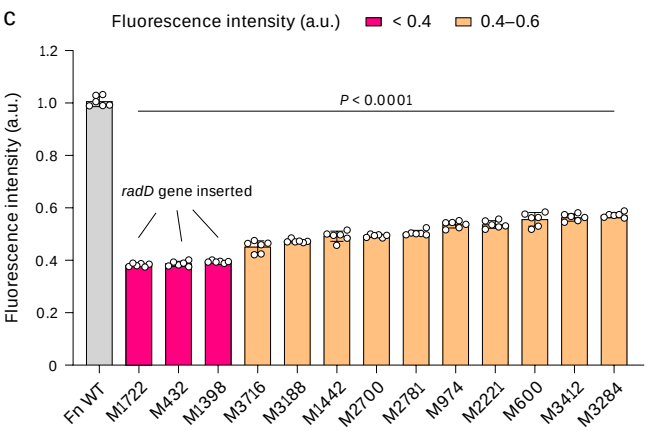


**Fig. 1 | High-throughput screen to identify the genes necessary for *F. nucleatum* adherent to CRC cells. a**, Schematic pipeline of the high-throughput screen developed to identify the *F. nucleatum* genes involved in adherence to CRC cells. **b**, The fluorescence intensity (in arbitrary units, a.u.) of ~4,000 clones from the transposon library. Each dot represents the mean of two biological replicates per sample. **c**, The results of the second round of screening for 13 mutants with the most significantly decreased fluorescence intensity (in a.u.); $n = 6$ biological replicates in each group. Data are presented as mean ± s.e.m. from three independent experiments. *P* values (all mutants compared with Fn WT, $P < 0.0001$) were determined by one-way ANOVA with Dunnett's test in **c**. Scheme in **a** was partially created with BioRender.com.

to tumour-expressed D-galactose-β(1-3)-N-acetyl-D-galactosamine (Gal–GalNAc) and mediates *F. nucleatum* colorectal adenocarcinoma enrichment[27]. Nevertheless, the adhesive potential of *F. nucleatum* persists even in mutants lacking both FadA and Fap2[28]; whether there are additional CRC-associated adhesins in *F. nucleatum* remains poorly understood.

Based on genome-wide transposon insertion screen, we identified three *F. nucleatum* mutants with severely defective adhesion to CRC cells, all of which had the *radD* gene inactivated by insertion, suggesting that RadD may be involved in tumour cells binding. As previously reported, RadD is recognized as a major anchor for polymicrobial interaction, co-aggregation and biofilm formation, which can be inhibited

by arginine and lysine[29–32]. Mutants devoid of *radD* show severe defects in inducing cell death in immortalized human T lymphocytes[33]. In addition, RadD has been shown to be involved in lysine metabolism and to modulate bacterial virulence in a mouse model of infection[32]. However, whether RadD could directly bind to tumour cells and its potential pro-tumorigenic effect in CRC have been under-explored.

In this Article, we demonstrated that RadD facilitated *F. nucleatum* attachment to CRC cells and determined its role in promoting tumorigenesis via specific binding to tumour-expressed CD147. The RadD–CD147 interaction mediates the enrichment of *F. nucleatum* within CRC tissues, activating an oncogenic PI3K–AKT–NF–κB cascade that enhances colorectal carcinogenesis. Furthermore, our findings suggest that targeting RadD–CD147 axis could be a potential strategy for CRC treatment.

## Results

### Genome-wide screen of *F. nucleatum* genes for CRC attachment

To identify genes necessary for *F. nucleatum* adherence to CRC cells, we generated a random mutagenesis library using the *mariner*-based transposon system, which is particularly suitable for high-AT (adenine and thymine)-content bacteria such as fusobacteria (Extended Data Fig. 1a,b). Approximately 4,000 clones from the library were labelled with the fluorescent dye fluorescein isothiocyanate (FITC) and co-incubated with the CRC cell line HCT116 in a 96-well plate. Non-adherent bacteria were washed away. The fluorescence intensity of each well, indicating the adhesion ability of each clone to HCT116 cells, was measured using a fluorescent microplate reader (Fig. 1a). We observed that the fluorescence intensity of 13 clones decreased by more than 40%, among which three independent clones (M432, M1398 and M1722) showed the most significant decrease (about 60%) (Fig. 1b,c).

Interestingly, the transposon location analysis revealed that all three clones harboured the transposon within the same 10.4 kb gene (positions 1,160/1,161 bp, 2,293/2,294 bp and 4,744/4,745 bp, respectively), corresponding to *radD*, encoding an autotransporter protein in *F. nucleatum* ATCC 23726 (Extended Data Fig. 1c and Supplementary Table 1). The predicted RadD protein structure by AlphaFold2 showed a distinctive ring shape (Extended Data Fig. 1d,e), sharing homology with typical type Va autotransporters, known for their essential involvement in the colonization and virulence in Gram-negative bacteria.

Next, to visualize the impaired cell binding caused by *radD* mutation, *F. nucleatum* wild type (Fn WT) and all three mutants were FITC stained and incubated with HCT116 cells. Confocal fluorescence microscopy showed that adherence in all three *radD* mutants was 2.8- to 3.3-fold lower than the wild-type strain (Extended Data Fig. 1f,g). These results strongly suggest RadD's involvement in mediating the adhesion between *F. nucleatum* and CRC cells.

### *F. nucleaum* RadD mediates adhesion of CRC cells and tissues

To avoid potential polar effects resulting from transposon insertion, we performed a markerless knockout of the *radD* gene in Fn WT, yielding strain Fn Δ*radD* (Extended Data Fig. 2a,b). We observed that the growth of Fn Δ*radD* was comparable to Fn WT and the complementation strain Fn Δ*radD/radD*, indicating that *radD* deletion did not affect the growth of the strains (Extended Data Fig. 2c).

Attachment and invasion are the hallmarks of *F. nucleatum*. Flow cytometry analysis revealed a markedly reduced adhesion of Fn Δ*radD* to HCT116 cells compared with both Fn WT and Fn Δ*radD*/*radD* (Fig. 2a). Confocal fluorescence microscopy and fluorescent microplate reader analysis confirmed these results (Fig. 2b–e,h). Furthermore, transmission electron microscopy (TEM) showed a decreased number of bacteria adhering to the cell surface or residing in the cytoplasm in the Fn Δ*radD*-treated group (Fig. 2f,g). These data suggest that RadD promotes the adhesion and invasion of *F. nucleatum* to CRC cells, with its absence markedly attenuating this interaction.

To extensively explore RadD-mediated attachment, eight human and mouse CRC cell lines underwent flow cytometry analysis after co-incubation with Fn WT, Fn Δ*radD* and Fn Δ*fap2*, respectively. As depicted in Extended Data Fig. 2d–k, the adhesion ability of Fn Δ*radD* and Fn Δ*fap2* to eight CRC cell lines decreased to varying degrees compared with that of Fn WT. In addition, invasion capabilities were assessed by plate counting. We observed that the invasive ability of Fn Δ*radD* and Fn Δ*fap2* was comparable, but both were significantly weaker than Fn WT (Extended Data Fig. 2l–s). Our data suggest that RadD might bind to a receptor ubiquitously expressed on the surface of CRC cells to facilitate the adhesion and invasion of *F. nucleatum*.

With further analysis using tissue sections, we observed that Fn Δ*radD* showed diminished attachment to both human and mouse CRC sections compared with Fn WT (Extended Data Fig. 3). However, on normal colorectal tissues, Fn WT and Fn Δ*radD* showed similar adhesion ability, although notably weaker than that on CRC tissues. These results suggest that RadD might bind to a receptor specifically expressed on CRC cells rather than normal colon epithelial cells.

### RadD exerts pro-CRC tumorigenesis effects in *Apc*$^{Min/+}$ mice

We next sought to investigate whether RadD could promote CRC cell proliferation. In Cell Counting Kit 8 assays, Fn Δ*radD* and Fn Δ*fap2* showed a significantly weaker ability to promote cell proliferation compared with Fn WT (Fig. 3a,b and Extended Data Fig. 4a,b). This observation was further supported by 5-ethynyl-2′-deoxyuridine (EdU) and colony formation assays (Extended Data Fig. 4c,d,g,h). In addition, transwell and scratch wound assays revealed that Fn Δ*radD* or Fn Δ*fap2* treatment resulted in fewer cells crossing the membrane after degrading the matrigel matrix and slower wound healing (Extended Data Fig. 4e,f,i,j). Moreover, in subcutaneous tumour-bearing BALB/c nude mice, we observed slower tumour growth in both Fn Δ*radD* and Fn Δ*fap2* treated groups compared with Fn WT (Fig. 3c–f and Extended Data Fig. 4k–m). These results suggest that RadD is necessary for *F. nucleatum* to promote the proliferation of CRC cells.

Next, *Apc*$^{Min/+}$ mice (a genetic mouse model of spontaneous CRC) were used to further explore the influence of RadD on colorectal tumorigenesis (Fig. 3g). Representative colon images are shown in Fig. 3h. As expected, Fn WT notably accelerated the development of CRC. By contrast, *Apc*$^{Min/+}$ mice treated with Fn Δ*radD* or Fn Δ*fap2* showed less tumour multiplicities and tumour weight compared with those treated with Fn WT (Fig. 3i,j). Quantitative PCR (qPCR) and fluorescence in situ hybridization (FISH) confirmed that deletion of *radD* or *fap2* greatly reduced *F. nucleatum* colonization in colorectal tumours (Fig. 3k,o). Immunohistochemistry (IHC) also showed the less Ki-67$^{+}$ cells in colon tumours of Fn Δ*radD* or Fn Δ*fap2* treated group (Fig. 3l,m). Histological verification of all colonic tumours revealed a markedly high incidence of dysplasia in *Apc*$^{Min/+}$ mice treated with Fn WT in contrast to those treated with Fn Δ*radD* or Fn Δ*fap2* (Fig. 3n). In addition, co-administration of Fn WT and Fn Δ*radD* further confirmed the involvement of RadD in *F. nucleatum* colonization of colonic tumour tissues (Fig. 3p). Collectively, these results suggest that RadD is important for the localization and enrichment of *F. nucleatum* in colonic tumour tissues, thereby exerting its oncogenic effect in *Apc*$^{Min/+}$ mice.

### Elevated *radD* levels correlated with poor patient outcomes

To examine the potential relationship between the prevalence of the *radD* gene and colorectal carcinogenesis, we conducted a meta-analysis incorporating data from three published studies of CRC. This dataset encompassed faecal metagenomic information from 166 cancer cases and 146 tumour-free controls (Supplementary Data 1)[14,34,35]. After applying consistent data reprocessing according to hidden Markov models and co-abundance clustering, we found the *radD* gene was clearly and consistently detected in deeply sequenced faecal metagenomes and showed significant enrichment in CRC groups across all three studies (Fig. 4a–c).

https://doi.org/10.1038/s41564-024-01784-w

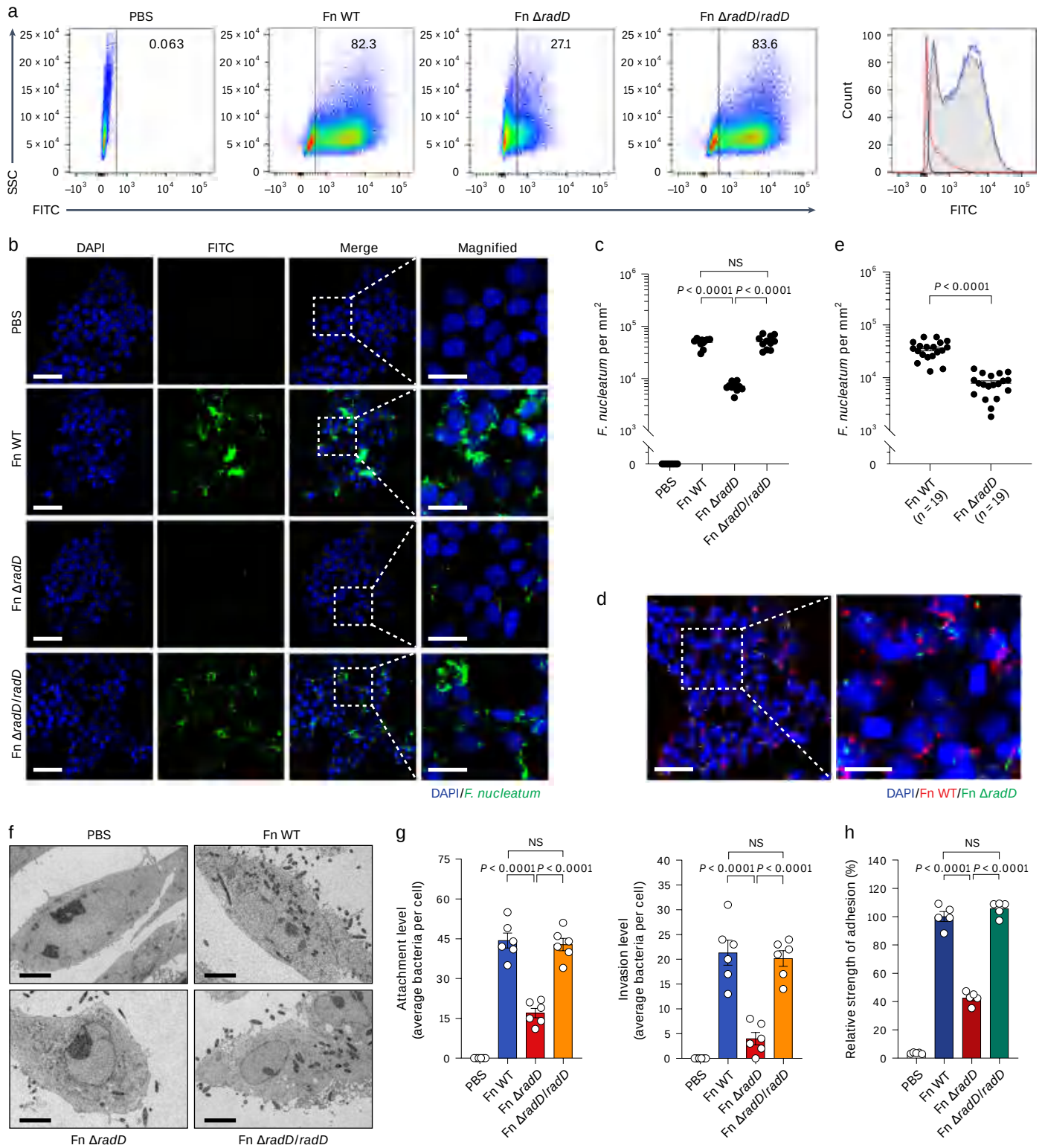


**Fig. 2 | RadD is involved in the attachment of *F. nucleatum* to CRC cells.** **a**, Flow cytometry analysis of *radD*-deficient mutant that was impaired in binding to human CRC cell line HCT116. The peaks for each group are displayed in the histogram on the right: black, PBS; grey-filled, Fn WT; red, Fn Δ*radD*; blue, Fn Δ*radD*/*radD*. SSC, side scatter. Data are representative of three independent experiments. **b**, Representative images of FITC-labelled (green) Fn WT, Fn Δ*radD* and Fn Δ*radD*/*radD* attachment to DAPI-stained (blue) HCT116 cells. Scale bars, 50 μm (leftmost column) and 20 μm (magnified images, rightmost column). **c**, Quantitation of *F. nucleatum* binding performed in **b** ($n = 11$ biological replicates in each group). **d**, Representative confocal images showing FITC-labelled Fn Δ*radD* (green) and Cy3-labelled Fn WT (red) binding to DAPI-stained (blue) HCT116 cells. Scale bars, 50 μm (left panel) and 20 μm (magnified image, right panel). **e**, Quantitation of *F. nucleatum* binding performed in **d** ($n = 19$ biological replicates). **f**, Representative TEM images of Fn WT, Fn Δ*radD* and Fn Δ*radD*/*radD* attaching and invading into HCT116 cells. Scale bars, 5 μm. **g**, Quantification of *F. nucleatum* binding and invading in **f** ($n = 6$ biological replicates). **h**, Fluorescence microplate reader analysis of the attachment of Fn WT, Fn Δ*radD* and Fn Δ*radD*/*radD* to HCT116 cells ($n = 5$ biological replicates). Data are presented as mean ± s.e.m. from three independent experiments. *P* values were determined by paired two-tailed Student's *t*-test in **e** and by one-way ANOVA with Turkey's test in **c**, **g** and **h**.

To evaluate the involvement of *radD* in fusobacteria localization within CRC, we analysed the abundance of the *radD* gene in both CRC and adjacent noncancerous tissues from 18 patients in cohort 1 (Supplementary Table 2). The qPCR results showed a notable elevation of *radD* gene abundance (*radD* gene normalized to Fn 16S ribosomal RNA) in CRC tissues compared with that in noncancerous controls, which was consistent with the results for another adhesin gene *fap2* ($P = 0.0465$) but had a lower $P$ value ($P = 0.0151$) (Fig. 4d). These findings imply that the high abundance of the *radD* gene might facilitate *F. nucleatum* CRC enrichment.

Next, we investigated the relationship between the abundance of the *radD* gene and American Joint Committee on Cancer (AJCC) stage in cohort 2 (Supplementary Data 2). When the *radD* gene levels were normalized to Fn 16S rRNA to reflect *radD* abundance in *F. nucleatum*, a stepwise increase corresponding to the AJCC stage was observed (Fig. 4e), indicating that *radD*-positive *F. nucleatum* might contribute to CRC progression. Furthermore, to assess the clinical relevance of the *radD* gene level, we analysed the different clinicopathological features in an additional cohort (cohort 3), who exhibited similar *F. nucleatum* abundance (Supplementary Data 3). Within cohort 3, samples were stratified into subsets characterized by high and low-*radD* abundance (cut-off value −16.5[−deltaCT value = Ct GAPDH - Ct *radD*]). Notably, the high-*radD* group exhibited larger tumour sizes compared with those of the low-*radD* group. In addition, a positive correlation between the abundance of *radD* and AJCC stage was observed. Moreover, we found that the risk of CRC recurrence was higher in the high-*radD* group compared with those in the low-*radD* group (Fig. 4f,g). Univariate and multivariate regression analyses revealed that the *radD* gene level was an independent risk factor of CRC aggressiveness (Supplementary Fig. 1). Our data indicate that the abundance of *radD* gene is clinically associated with CRC progression.

## RadD mediates *F. nucleatum* CRC enrichment by binding CD147

Identifying host cell receptors capable of binding to RadD is critical to gain an insight into the pathogenesis of *F. nucleatum*. L-Arginine and L-lysine, inhibitors of RadD-mediated bacterial co-aggregation, significantly reduce the adhesion of RadD to CRC cells. Sugar molecules such as galactose, sialic acid and mannose reduced the adhesion of Fn WT, but they did not ablate adhesion in either genotype (Extended Data Fig. 5a). Therefore, a combined genetics and proteomics approach was performed (Extended Data Fig. 5b–f). Briefly, the membrane proteins of Fn Δ*radD* and the overexpression strain Fn WT-*radD* were labelled with biotin, followed by incubating with streptavidin beads, which has an extremely high affinity for biotin. Complex 1 (streptavidin beads–biotin–Fn WT–*radD* membrane protein) and complex 2 (streptavidin beads–biotin–Fn Δ*radD* membrane protein) were formed and then co-incubated with HCT116 cell membrane proteins. Unbound proteins were removed by extensive washing. Finally, the top 20 enriched cell membrane proteins that were specifically bound by complex 1 were obtained using mass spectrometry and differential analysis (Supplementary Data 4).

To further screen potential receptors, we designed 20 specific small interfering RNAs (siRNAs) to individually target the candidate genes. Upon transfection of HCT116 cells with siCD147, a dramatic reduction in the number of adherent Fn WT was observed, while knockdown of ITGB1 or ANXA4 showed a moderate reduction, compared with cells transfected with control siRNAs (Extended Data Fig. 5g). Moreover, the binding of Fn WT notably increased when CD147 was overexpressed (Extended Data Fig. 5h). A second siRNA targeting *CD147* was designed, and consistent results were obtained in both HCT116 and SW480 cells (Fig. 5a–c and Extended Data Fig. 6a–c). These data indicate that CD147 is the primary receptor for RadD among these candidates.

Subsequently, fluorescent confocal microscopy revealed high co-location rates of FITC-labelled Fn WT with CD147 in HCT116 and SW480 cells, and the reduction of CD147 surface expression correlated with the decreased adhesion of Fn WT to both cell lines (Fig. 5d,e and Extended Data Fig. 6d,e). Moreover, preincubation of cells with recombinant CD147 proteins or anti-CD147 antibodies before infection inhibited the attachment of Fn WT, whereas it had no effect on the adhesion of Fn Δ*radD* (Fig. 5f–i and Extended Data Fig. 6f–i). Consistent with the in vitro cellular models, blocking CD147 on tissue sections from two patients with advanced CRC substantially reduced the adhesion of Fn WT (Extended Data Fig. 6j,k). Co-immunoprecipitation experiments further confirmed that RadD and CD147 could directly bind to each other (Fig. 5j,k). Overall, these data confirm that RadD mediates *F. nucleatum* attachment to CRC cells through its surface protein RadD binding to CD147 receptor.

Next, we sought to explore whether elevated levels of CD147 are associated with an increasing colonization of RadD-expressing *F. nucleatum* in CRC tissues. Through combined IHC and qPCR analyses, we observed the abundance of *radD* gene showed a stepwise increase that correlated with the clinical grade and the expression level of CD147 (Fig. 5l–n), suggesting specific interaction between fusobacterial RadD and tumour-expressed CD147, potentially leading to the localization and enrichment of *F. nucleatum* in CRC tissues.

Phylogenetic analysis revealed the presence of RadD in various *Fusobacterium* species, predominantly within *F. nucleatum* subspecies (Extended Data Fig. 7a). *F. nucleatum* subsp. *polymorphum* strain ATCC 10953 (Fn10953), which allows for effective genetic manipulation, was further used to explore RadD-mediated CRC binding. Similar to the effect observed with Fn23726, *radD* gene inactivation or CD147 blocking reduced the adhesion of Fn10953 to CRC cells (Extended Data Fig. 7b–i). These findings confirm that RadD–CD147 interaction facilitates *F. nucleatum* CRC attachment, a mechanism that may also extend to other fusobacteria.

**Fig. 3 | *F. nucleatum* RadD induces cell proliferation and promotes colonic tumorigenesis in *Apc*$^{Min/+}$ mice. a**, HCT116 cell proliferation was determined by Cell Counting Kit 8 assay (CCK8). **b**, Fn WT stimulated the proliferation of HCT116, compared with those treated with Fn Δ*radD* or Fn Δ*fap2* ($n = 3$ biological replicates in each group). Data were repeated with three independent experiments. **c**, Experimental procedure for intratumoural bacteria injection in the subcutaneous tumour model. **d**, Representative images of HCT116 subcutaneous tumours following intratumoural injection of the indicated bacteria in BALB/c nude mice. **e**,**f**, Tumour volume ($mm^3$) (**e**) and weight (**g**) (**f**) were measured ($n = 9$ mice per group). **g**, Schematic diagram showing the experimental design of the *Apc*$^{Min/+}$ mouse model. **h**, Representative colonic morphologies of *Apc*$^{Min/+}$ mice from different treatment groups. The colonic tumors are indicated by red arrows. **i**,**j**, Colonic tumour number (**i**) and tumour weight (**j**) of *Apc*$^{Min/+}$ mice were measured ($n = 9$ mice per group). **k**, *F. nucleatum* abundance in matched tumour (T) versus normal (N) tissues from colons of *Apc*$^{Min/+}$ mice measured by qPCR. ND, not detected. **l**,**m**, IHC was performed to detect Ki-67$^+$ cells in colon tumours (**l**) and statistically analysed using the immunohistochemical immunoreactive score of Remmele and Stegner (IRS) (**m**). Scale bars, 50 μm. **n**, Percentage (%) of normal or HGD colon samples in each group based on histological scores. HGD, high-grade dysplasia. $n = 9$ biologically independent samples per group. **o**, FISH was performed to detect *F. nucleatum* in colonic tumours of *Apc*$^{Min/+}$ mice. Fn WT or Fn Δ*radD* in tumours is indicated by white arrows. Scale bars, 50 μm. Three independent experiments were repeated showing similar results. **p**, *Apc*$^{Min/+}$ mice colonic tumour enrichment of Fn WT and Fn Δ*radD* inoculated as a mixture ($n = 18$ mice). Data are presented as mean ± s.e.m. $P$ values were determined by two-way ANOVA with Turkey's test in **b** and **e**, one-way ANOVA with Turkey's test in **f**, **i**, **j**, **k** (comparison of tumour tissues among three different groups) and **m**, and paired two-tailed Student's $t$-test in **k** (comparison between tumour and normal tissues in each group) and **p**. Schemes in **a**, **c** and **g** were partially created with BioRender.com.

https://doi.org/10.1038/s41564-024-01784-w

### RadD–CD147 interaction triggers oncogenic signalling cascades

To explore the downstream signalling pathway mediated by RadD and CD147 interaction, we performed gene expression profiling of HCT116 cells co-incubated with Fn WT or Fn Δ*radD*. RNA sequencing (RNA-seq) revealed that 226 genes were significantly upregulated after Fn WT treatment compared with Fn Δ*radD* treatment. Further gene enrichment analysis revealed that the RadD-dependent upregulated genes were associated with pathways involving redox homeostasis, PI3K–AKT–NF-κB and lipid metabolism (Fig. 6a,b and Supplementary Data 5).

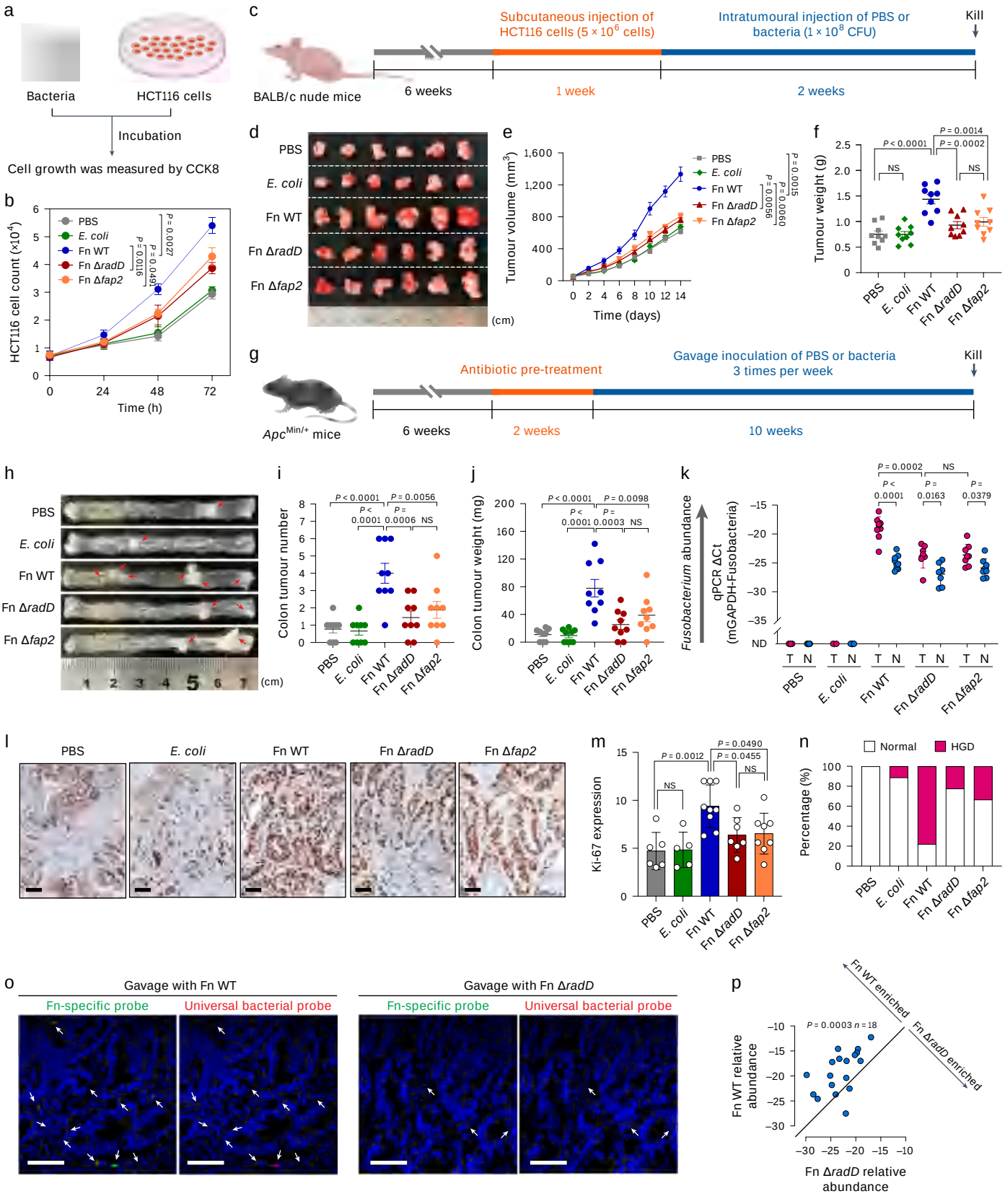

https://doi.org/10.1038/s41564-024-01784-w

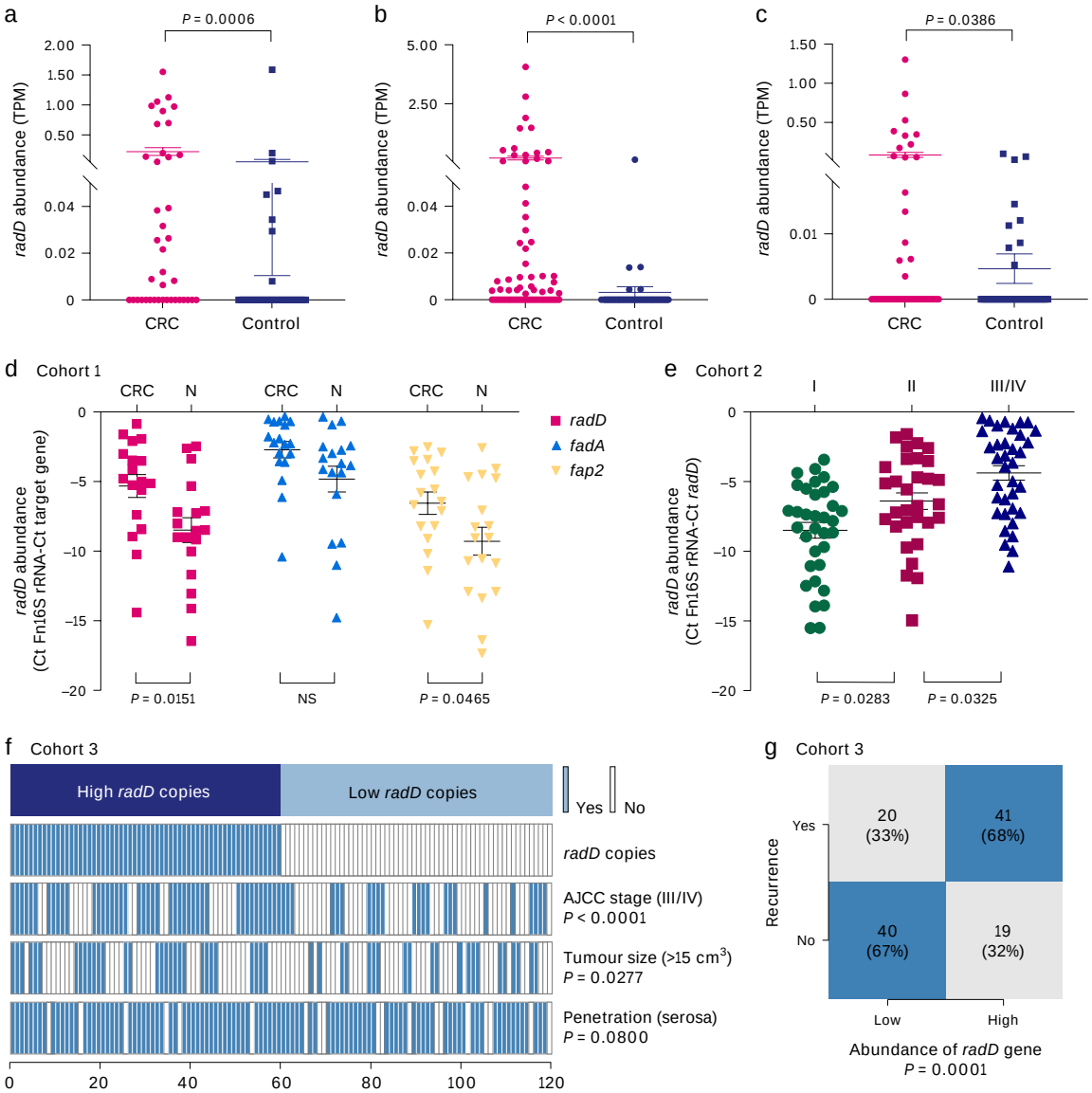


**Fig. 4 | High abundance of *radD* gene correlates with increased risk of CRC.** **a**–**c**, The normalized abundance of the *radD* gene was compared between metagenomes of both control and CRC cases from the Japan (**a**) (control, $n = 40$ independent samples; CRC, $n = 40$ independent samples), China (**b**) (control, $n = 54$ independent samples; CRC, $n = 74$ independent samples) and US (**c**) (control, $n = 52$ independent samples; CRC, $n = 52$ independent samples) study populations. TPM, transcripts per kilobase million. **d**, Statistical analysis of *F. nucleatum radD*, *fadA* and *fap2* gene abundance (target gene normalized to Fn 16S ribosomal RNA) in noncancerous controls ($n = 18$ independent samples) and CRC tissues ($n = 18$ independent samples), cohort 1. Ct, cycle threshold. **e**, The abundance of the *radD* gene (*radD* gene normalized to Fn 16S ribosomal RNA) in CRC tissues was subjected to statistical analysis based on AJCC stage (stage I, $n = 34$ independent samples; stage II, $n = 31$ independent samples; stage III/IV, $n = 36$ independent samples), cohort 2. **f**, Comparison of AJCC stage, tumour size and positive or negative serosal invasion between high-*radD* ($n = 60$ independent samples) and low-*radD* ($n = 60$ independent samples) tumours of cohort 3. **g**, Statistical analysis was performed based on the abundance of *radD* and recurrence rate in cohort 3. Data are presented as mean ± s.e.m. *P* values were determined by two-tailed Mann–Whitney test in **a**–**c**, paired two-tailed Student's *t*-test and Wilcoxon signed rank test in **d**, one-way ANOVA with Turkey's test in **e**, and chi-square test in **f**.

Preliminary studies have reported that CD147 plays a central role in driving the proliferation, invasion and metastasis of tumour cells by activating the PI3K/AKT and NF-κB pathways and stimulating the secretion of matrix metalloproteinases (MMPs) from cancer cells[36–38]. Hence, we speculate that *F. nucleatum* promotes the PI3K–AKT–NF–κB–MMP9 signalling axis via the RadD–CD147 interaction, consequently enhancing CRC tumorigenesis (Fig. 6c). To test this, we silenced the PI3K/AKT pathway in HCT116 cells and observed that the pro-tumorigenic effect induced by Fn WT was reduced to a level comparable to that of Fn Δ*radD* (Extended Data Fig. 8a–d). In addition, despite that FadA-associated Wnt/β–catenin signalling pathway was reported to stimulate CRC cell proliferation, we found RadD's pro-tumorigenic effect may not depend on this pathway (Extended Data Fig. 8e–g). These results confirm that RadD mediated the pro-tumorigenic phenotype mainly through the activation of the PI3K signalling pathway.

To substantiate this, the messenger RNA expression levels of genes implicated in the PI3K–AKT–NF–κB–MMP9 pathway were detected. Notably, five pivotal genes, including *PIK3R2*, *AKT1*, *NFKB1*, *MMP2* and *MMP9*, as well as *PCNA* (a marker of cell proliferation), showed significant upregulation in Fn WT-treated CRC cells (Fig. 6d and Extended Data Fig. 8h–m). Consistently, their total or phosphorylated protein levels were also markedly upregulated, as determined by western

https://doi.org/10.1038/s41564-024-01784-w

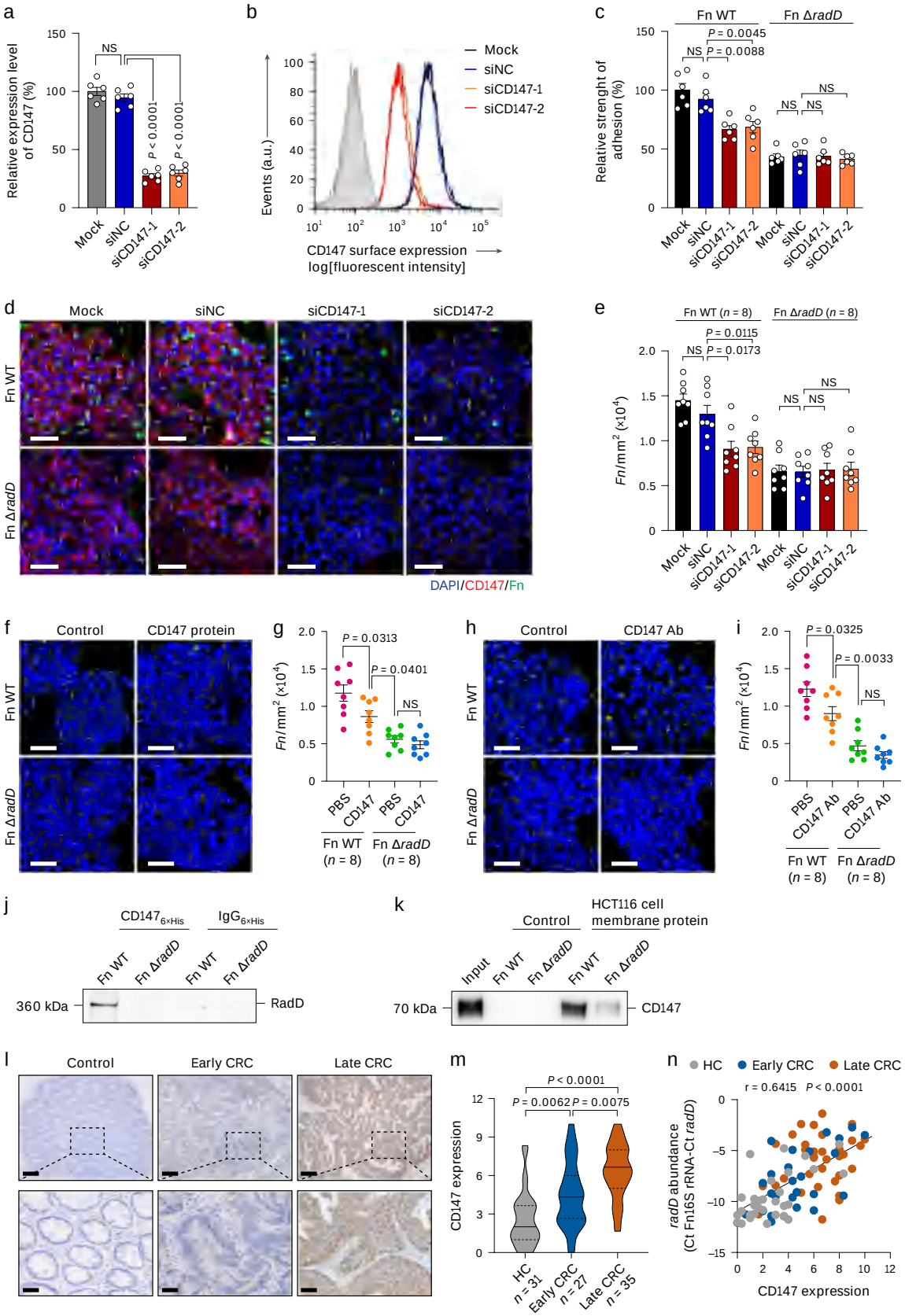


blotting. Furthermore, co-treatment with CD147 antibodies notably attenuated the RadD-induced PI3K–AKT–NF-κB–MMP9 signalling cascades (Fig. 6e and Extended Data Fig. 8n–r). In addition, we observed that patients in cohort 3 with a higher level of the *radD* gene were more likely to exhibit elevated levels of PI3K p85, p-PI3K p85, p-AKT, PCNA and MMP9 (Fig. 6f,g). Altogether, these results suggest that *F. nucleatum* activates the PI3K–AKT–NF-κB–MMP9 signal transduction pathway through the RadD–CD147 interaction.

**Fig. 5 | *F. nucleatum* RadD attaches to CRC cells and tissues by interacting with tumour-expressed receptor CD147. a**,**b**, RT-qPCR (**a**) and FACS (**b**) analysis of CD147 expression in HCT116 cells, with siNC as a negative control ($n = 6$ biological replicates in each group). **c**, The relative levels of attachment of Fn WT and Fn Δ*radD* to CD147-depleted HCT116 cells ($n = 6$ biological replicates). **d**, Immunofluorescence analysis of FITC-labelled Fn WT and Fn Δ*radD* attachment to CD147-depleted HCT116 cells. Scale bars, 50 μm. **e**, Quantitation of *F. nucleatum* binding performed in **d** ($n = 8$ biological replicates). **f**,**g**, Representative confocal images (**f**) and quantitation (**g**) of FITC-labelled (green) Fn WT and Fn Δ*radD* binding to DAPI-stained (blue) HCT116 cells preincubated with soluble CD147 proteins ($n = 8$ biological replicates). Scale bars, 50 μm. **h**,**i**, Representative images (**h**) and quantitation (**i**) of FITC-labelled (green) Fn WT and Fn Δ*radD* attachment to DAPI-stained (blue) HCT116 cells preincubated with anti-CD147 antibodies ($n = 8$ biological replicates). Scale bars, 50 μm. **j**, Commercial recombinant CD147 (6×His tag) coprecipitation with RadD after incubating with cell membrane proteins of Fn WT or Fn Δ*radD*; IgG was used as the negative control. **k**, Biotin-labelled Fn WT or Fn Δ*radD* coprecipitation with CD147 proteins after incubating with cell membrane proteins of HCT116 cells. **l**, Representative IHC of CD147 expression level in healthy control (HC) and early and late CRC tissues according to AJCC stage. Scale bars, 200 μm (upper panels) and 50 μm (magnified images, lower panels). **m**, Statistical analysis of the CD147 expression level using the immunohistochemical immunoreactive score of Remmele and Stegner (IRS) (HC, $n = 31$ independent samples; early CRC, $n = 27$ independent samples; late CRC, $n = 35$ independent samples). The median is indicated with the solid line, and 25th and 75th percentiles are indicated with dashed lines in the violin plot. **n**, CD147 expression level ($x$-axis) versus *radD* gene abundance (*radD* gene normalized to Fn 16S ribosomal RNA) in tissues ($y$-axis) is plotted. Ct, cycle threshold. Each symbol represents data from one patient. The Spearman correlation coefficient value and $P$ value are shown. Data are presented as mean ± s.e.m. from three independent experiments. $P$ values were determined by one-way ANOVA with Turkey's test in **a**, **g**, **i** and **m** and Dunnett's test in **c** and **e**.

### Blocking RadD–CD147 reduces *F. nucleatum*'s pro-tumour effects

To verify the role of RadD–CD147 interaction in the promotion of cell proliferation, we blocked CD147 with antibodies in cells before co-incubation with Fn WT or Fn Δ*radD*. Functional assays revealed that the addition of CD147 antibodies notably decreased the proliferation-enhancing capability of RadD on CRC cells (Extended Data Fig. 9a–j). Moreover, in HCT116 or SW480 tumour-bearing BALB/c nude mouse, we observed a notable reduction in tumour size and weight, as well as downregulation of PI3K–AKT–NF–κB–MMP9 signalling cascades in Fn WT-treated mice injected with CD147 antibodies compared with the control group (Extended Data Fig. 9k–x). These results suggest that blocking RadD–CD147 interaction weakens *F. nucleatum*' role in promoting CRC cell proliferation.

In $Apc^{Min/+}$ mouse models, blocking CD147 with antibodies significantly reduced the tumour burden in both colon and small intestine in the Fn WT-treated group, while showing little effect on the control or Fn Δ*radD*-treated group (Fig. 6h–k and Extended Data Fig. 10a,b). Real-time quantitative PCR (RT-qPCR) and IHC analysis further revealed that CD147 antibodies downregulated the expression levels of *Pik3r2*, *Akt1*, *Nfκb1* and *Mmp9* genes and decreased the levels of p-PI3K p85 and p-Akt induced by Fn WT (Extended Data Fig. 10c–j). Collectively, our data validate the underlying role of the RadD–CD147 interaction in activating PI3K–Akt–NF–κB signalling cascades in *F. nucleatum*-mediated colorectal tumorigenesis in $Apc^{Min/+}$ mice.

## Discussion

Increasing evidence suggests that *F. nucleatum*, a cancer-associated microbiota member, is enriched in stool and mucosal samples of patients with CRC, contributing to tumorigenesis[9,10,39–41]. Herein, through systematic genetic investigation, we identified RadD as a facilitator of *F. nucleatum* attachment to CRC and determined its role in promoting tumorigenesis.

Previous studies indicate that *F. nucleatum* RadD can co-aggregate with various gram-positive bacterial species[32,42–46] and fungal pathogens such as *Candida albicans*[47,48], enhancing biofilm formation. During our genome-wide screen, we were surprised to discover that inactivation of RadD resulted in impaired adhesion between *F. nucleatum* and CRC cells. Furthermore, previous reports suggest the expression of *radD* gene is regulated by the two-component system CarRS (coaggregation regulator and sensor), and inactivation of CarS (coaggregation sensor) leads to a defect in polymicrobial coaggregation[32]. In our transposon library, we also isolated a CarS-inactivated mutant (M3716) and observed a notable downregulation of *radD* expression, along with its adhesion deficiency phenotype with CRC cells (Supplementary Fig. 2). This suggests that RadD expression might be modulated by external signals, leveraging its multifaceted effects and engaging in various interactions with neighbouring bacteria and CRC tissues.

Published literature[28] and our study showed that deletion of *fadA* in *F. nucleatum* 23726 does not affect the adhesion and invasion ability of bacteria to CRC cells (Supplementary Fig. 3), possibly due to the presence of multiple *fadA* ortholog genes in this strain[28]. Hence, in our study, we focus on Fap2 and RadD and determine their roles in adhesion and cancer-promoting. Absence of either *fap2* or *radD* notably reduces *F. nucleatum*'s ability to adhere to and invade CRC cells, and knockout of both further weakens the phenotype (Supplementary Fig. 4), akin to their role in triggering cell death in Jurkat cells[30]. As two adhesins can more firmly attach to the host surface, this may greatly assist bacteria in colonizing various complex and variable environments within host and gaining a competitive advantage among microbial communities.

In this study, nude mice, an important model for preclinical research, were used to explore the potential promoting effect of *F. nucleatum* RadD on the proliferation of CRC cells. However, it is noteworthy that nude mouse model has limitations due to the lack of a fully functional immune system, and the tumours were grown subcutaneously rather than within the intestine. Therefore, the findings from this model may not accurately reflect the biological and therapeutic dynamics in humans. To address this, we have additionally substantiated the results with the $Apc^{Min/+}$ mouse model.

**Fig. 6 | Blockade of CD147 suppressed *F. nucleatum* RadD activating the PI3K–AKT pathway, and attenuated RadD-induced colonic tumorigenesis in mice. a**, Transcriptional profiling of HCT116 cells after incubating with Fn WT and Fn Δ*radD* for 24 h. **b**, Heat map showing 123 genes that are consistently downregulated and 31 genes consistently upregulated. Three biologically independent samples per group. **c**, Schematic diagram of RadD interacting with CD147 to activate the PI3K–AKT–NF–κB signalling pathway. **d**,**e**, RT-qPCR (**d**) and western blot (**e**) validation of CD147-PI3K–AKT–NF–κB signalling pathway activated by *F. nucleatum* RadD in HCT116 cells ($n = 3$ biological replicates). The effects were attenuated by adding anti-CD147 antibodies. These blots were from different membranes, each including loading controls, and a representative loading control is shown here; all uncropped images for all blots are provided as source data. **f**, Representative IHC of PI3K p85, p-PI3K p85, p-AKT, PCNA and MMP9 proteins in CRC tissues with low or high abundance of *radD* gene. Scale bars, 100 μm (left panels) and 50 μm (magnified images, right panels). **g**, Statistical analysis of immunohistochemical immunoreactive score of Remmele and Stegner (IRS) scores of PI3K p85, p-PI3K p85, p-AKT, PCNA and MMP9 proteins in CRC tissues with low ($n = 37$ independent samples) or high ($n = 41$ independent samples) abundance of *radD* gene. **h**,**i**, Colonic tumour number (**h**) and tumour weight (**i**) of $Apc^{Min/+}$ mice were measured ($n = 10$ mice per group). **j**,**k**, Small intestine tumour number (**j**) and tumour size (**k**) of $Apc^{Min/+}$ were measured ($n = 10$ mice per group). Data are presented as mean ± s.e.m. $P$ values were determined by one-way ANOVA with Turkey's test in **d**, **h** and **j**–**k**, Brown–Forsythe and Welch ANOVA test with Dunnett's test in **i** and unpaired two-tailed Student's $t$-test in **g**. Scheme in **c** was partially created with BioRender.com.

https://doi.org/10.1038/s41564-024-01784-w

L-Lysine and L-arginine have been reported to act as the inhibitors of RadD-mediated polymicrobial co-aggregation[31,49]. We found that lysine, but not disruption of lysine metabolism pathway, could affect the adhesion of RadD to CRC cells (Supplementary Fig. 5). Moreover, the fact that lysine and arginine can each block the RadD-mediated coaggregation and CRC attachment raises the possibility that these positively charged amino acids may alter RadD's spatial conformation and thereby interfere its binding to ligands.

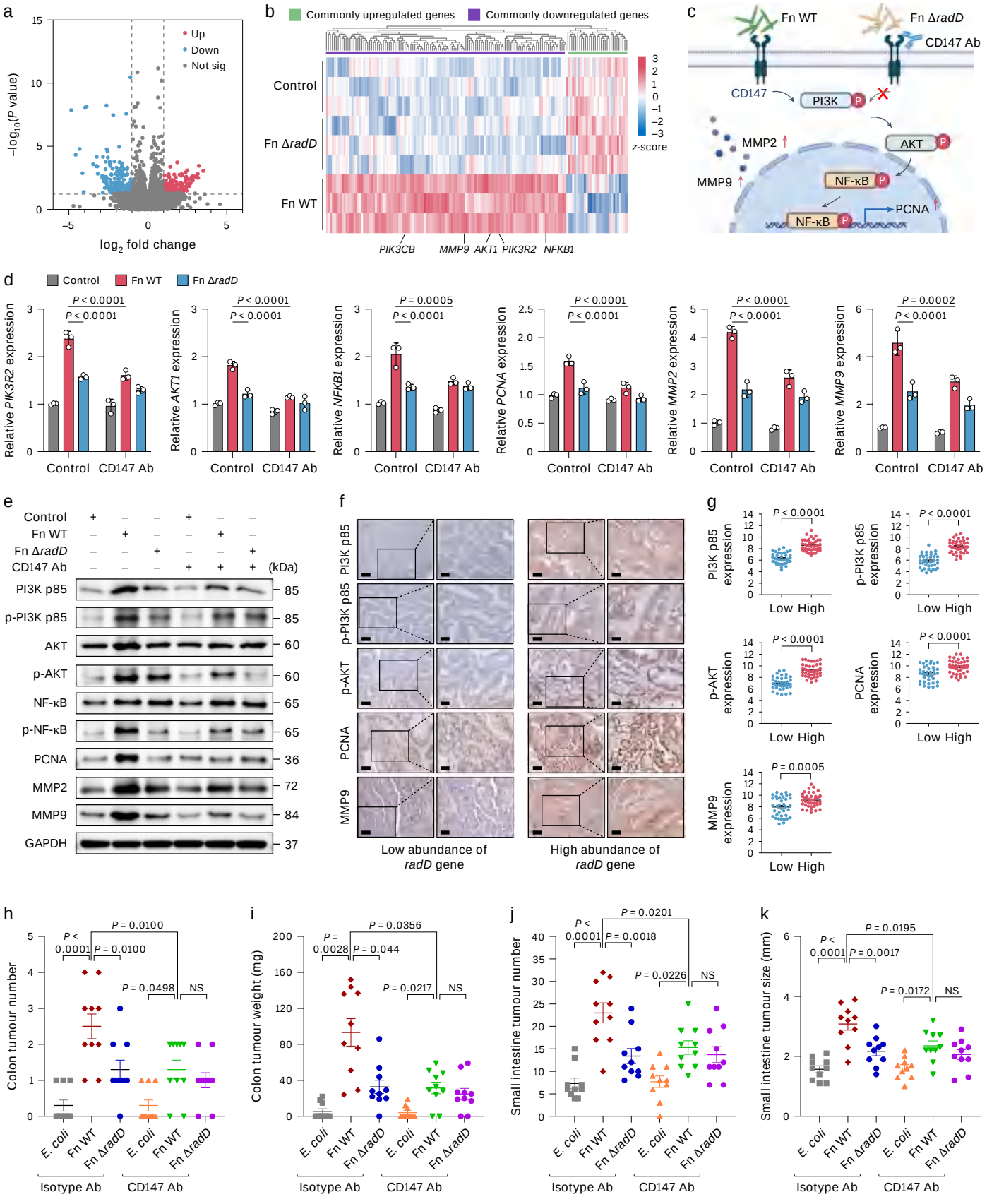

Notably, besides *F. nucleatum*, several other gastrointestinal human pathogens, including enteropathogenic *E. coli*[50], *Salmonella enterica* serovar Typhimurium[50], *Listeria monocytogenes*[51], and the meningococcal disease bacterial pathogen, *Neisseria meningitidis*[52], also target CD147 to adhere to and/or invade epithelial cells, indicating that CD147 is an evolutionarily conserved efficient target for pathogens infection. Moreover, our studies provide a potential mechanism that elevated levels of CD147 in adenocarcinomas compared with that in normal colonic mucosa might facilitate pathogens tumour-specific binding.

Our study has the following limitations. While multiple clinical covariates are considered in this study when analysing the potential association of *F. nucleatum* or adhesion genes to CRC, a recent publication suggests that the association of *F. nucleatum* to CRC may be driven by its link to intestinal inflammatory conditions, such as elevated faecal calprotectin levels[53]. Therefore, more inflammation-related covariates warrant further investigation to better understand these associations. In addition, given tumour niche-enriched strains predominantly belong to *F. nucleatum* subsp. *animalis* C2 (*Fna* C2)[54], further validations are needed to explore RadD-mediated colonization of *F. nucleatum* in tumours within clinically relevant subspecies.

## Methods

### Mouse models

The Shanghai Model Organisms Center, Institutional Animal Care and Use Committee approved all of the animal experiments conducted in this study. Mice were kept (no more than five per cage) in a specific pathogen-free facility at 20–26 °C and 40–70% humidity, following a cycle of 12 h light/12 h dark, with free access to food and water. No statistical methods were used to pre-determine sample sizes, but our sample sizes are similar to those reported in previous publications[8]. The mice were randomly assigned to different groups for the experiments, and no animals were excluded from the analyses. Data collection and analysis were not conducted in a blinded manner.

BALB/c nude mice (male, about 6 weeks old) were purchased from Shanghai Model Organisms. CRC cells ($5 \times 10^6$ HCT116 or SW480 cells) were subcutaneously injected into the right axilla of the BALB/c nude mice to establish the xenograft model. After 1 week, the mice were randomly assigned to various groups for different experimental sets. The group sizes were 9 mice per condition. Bacteria ($1 \times 10^8$ c.f.u. (colony-forming units)) or PBS were intratumourally injected, and anti-CD147 antibodies (50 μg per mouse) were delivered intraperitoneally twice a week. The tumour volume was assessed every other day using vernier calipers and calculated using the formula (length × width × width)/2.

*Apc*$^{Min/+}$ mice (male, about 6 weeks old) were obtained from Jackson Laboratory (catalogue number 002020). An antibiotic cocktail in drinking water (1 g $l^{-1}$ metronidazole, 1 g $l^{-1}$ ampicillin,1 g $l^{-1}$ neomycin, and 0.5 g $l^{-1}$ vancomycin) was provided for 14 days before oral gavage. After 2 weeks, the mice were randomly allocated to several groups according to the experimental requirements. The group sizes were 9–10 mice per condition. Bacteria ($1 \times 10^8$ c.f.u.) or PBS were administered by oral gavage every other day for 10 weeks. For CD147 blockade, anti-CD147 antibodies (50 μg, eBioscience, catalogue number 16-1471-025) or isotype control (50 μg, eBioscience, catalogue number 14-4321-85) were injected intraperitoneally twice a week for 10 weeks.

### Patients and clinical samples

The Renji Hospital Ethics Committee of Shanghai Jiao Tong University School of Medicine approved the clinical study protocol (KY2022-203-B). The entire research was conducted in compliance with the principles stated in the Helsinki Declaration of 1975 and its later amendments.

Three cohorts of patients with CRC from Renji Hospital affiliated to Shanghai Jiao Tong University School of Medicine between 2015 and 2020 were studied. Cohort 1 participants were collected from the Western Campus of Renji Hospital, and cohort 2 and cohort 3 participants were collected from the Eastern Campus of Renji Hospital. The patients' written informed consent, including consent to publish indirect identifiers (age, sex and diagnosis), was obtained from all participants. There was no patient compensation for participation in this study.

In cohort 1, we detected the abundance of Fn 16S rRNA, *radD*, *fadA* and *fap2* genes in 18 paired cancerous tissues and the adjacent normal tissues from patients with CRC (age mean, 63 years; 9 male and 9 female) using qPCR. The clinical characteristics of the study participants are shown in Supplementary Table 2.

In cohort 2, 101 patients with CRC (age mean, 62 years; 56 male and 45 female) were stratified into stages I, II and III/IV based on the AJCC staging criteria. The abundance of *radD* and Fn 16S rRNA in cancerous tissues were detected using qPCR. To reflect the relative abundance of *radD* in *F. nucleatum*, the amounts of the *radD* gene were normalized to that of Fn 16S rRNA. The clinical characteristics of the study participants are shown in Supplementary Data 2.

In cohort 3, we detected the relative abundance of *radD* genes in cancerous tissues from 120 CRC samples (age mean, 65 years; 68 male and 52 female) which showed similar *F. nucleatum* amount. The optimal cut-off value for *radD* abundance was determined by receiver operating characteristic analysis, and −16.5[−deltaCT value] was selected based on *radD* abundance that provided the best balance between sensitivity and specificity to predict efficacy. Samples were stratified into subsets characterized by high and low-*radD* abundance based on the threshold −16.5[−deltaCT value]. The clinical characteristics of the study participants, including the AJCC stage and tumour size in terms of the pathological report, as well as the recurrence-free rate of each patient were collected and are shown in Supplementary Data 3.

### Bacterial strains, plasmids and culture conditions

Bacterial strains and plasmids used in this study are listed in Supplementary Table 3. *F. nucleatum* subsp. *nucleatum* (ATCC 23726) and *F. nucleatum* subsp. *polymorphum* (ATCC 10953) were obtained from the ATCC. To facilitate genetic manipulation and virulence assessment of *F. nucleatum* ATCC23726, the galactokinase gene (*galK*) was deleted in the parental strain following previously published protocols[32,55,56]. As knockout of the *galK* gene does not affect the growth and virulence (Supplementary Fig. 6), the resulting *galK* mutant strain was used as the Fn WT throughout this study, and all gene-deleted strains were generated from this strain. *F. nucleatum* was cultured in TSPC (tryptic soy broth supplemented with peptone and cysteine) broth or agar at 37 °C in an anaerobic workstation[32]. *E. coli* strain DH5α was purchased from TIANGEN Biotech. It was grown in Luria–Bertani medium at 37 °C under aerobic conditions.

### Cell lines

The following human and mouse CRC cell lines were purchased from ATCC and The National Biomedical Cell-Line Resource of China: HCT116, SW480, RKO, DLD1, HT29, Caco2, MC38 and CT26. The specific culture conditions were as follows: HCT116 and HT29 cells were maintained in McCoy's 5A (Gibco, catalogue number 2323277) supplemented with 10% fetal bovine serum (FBS, Gemini, catalogue number 900-108). SW480 and DLD1 cells were cultured in RPMI 1640 medium (Gibco, catalogue number 8123275) supplemented with 10% FBS. RKO, Caco2, MC38 and CT26 cells were grown in DMEM (Gibco, catalogue number 8123298) supplemented with 10% FBS. All cell lines were placed in an incubator at 37 °C in an atmosphere of 5% $CO_2$.

### Construction of the transposon library

To establish the transposon library in *F. nucleatum*, the mariner transposon plasmid pTn-Himar1, which contains the hyperactive *Himar1* C9 transposase gene[57–59] and the *galK* gene, was electro-transformed to mutagenize *F. nucleatum*. All transformants were then selected on

TSPC agar plates supplemented with 5 μg ml$^{-1}$ thiamphenicol for 72 h. Subsequently, they were collected and plated onto TSPC agar plates containing 5 μg ml$^{-1}$ thiamphenicol and 0.5% 2-deoxy-D-galactose (2-DG) to induce plasmid loss for 72 h. Following selection, individual colonies from the plates were inoculated into 400 μl of TSPC broth containing 5 μg ml$^{-1}$ thiamphenicol and grown anaerobically at 37 °C for 18 h. Glycerol stocks of each mutant were prepared by adding an equal volume of 50% glycerol in TSPC (resulting in a final glycerol concentration of 25%) to the liquid cultures, which were then stored at −80 °C until use.

### Screening for *F. nucleatum* genes involved in adherence

To identify the fusobacterial adhesin responsible for binding to CRC cells, ~4,000 transposon mutants were selected from the transposon library and cultured in deep 96-well plates containing 500 μl TSPC broth with 5 μg ml$^{-1}$ thiamphenicol added. After being anaerobically grown overnight to an optical density at 600 nm ($OD_{600}$) of 1.0 (mid-log phase) at 37 °C, the bacterial pellets were collected by centrifugation (5,000 × *g*, 10 min, 4 °C) and washed twice with sterile PBS. Then, 500 μl FITC solution (0.1 mg ml$^{-1}$ in PBS, Yeasen Biotechnology, catalogue number 60514ES60) was added into each well, and the pellets were re-suspended by pipetting. The plates were wrapped in aluminium foil and placed on a shaker at 37 °C for 2 h. After three additional washes with PBS, 100 μl FITC-labelled bacteria were co-incubated with HCT116 cells grown in 96-well plates for 1 h at 37 °C in an incubator. Post incubation, the cells were subjected to two PBS washes, and the fluorescence intensity of each well was measured using a fluorescent microplate reader (FLUOstar Omega).

### Generation of the deletion mutants

To generate deletion mutants in *F. nucleatum*, we used a two-step homologous recombination process following established protocols[32]. In brief, two homologous arms, each approximately 1.5 kb in length and flanking the targeted gene, were amplified via PCR. These two DNA fragments were fused and subsequently cloned into the integrative vector pFJ-KO, which contains the *Clostridium perfringens* chloramphenicol acetyltransferase gene (*catP*) and *galK* gene. The resulting plasmid was then introduced into *F. nucleatum* by electroporation, and the integration of the plasmid into the bacterial chromosome through homologous recombination was selected on TSPC agar plates containing 5 μg ml$^{-1}$ thiamphenicol at 37 °C under anaerobic conditions. Next, integrants were plated on TSPC plates containing 0.5% 2-DG to initiate a second homologous recombination event. The resulting deletion mutants were further verified through PCR, Sanger sequencing and/or western blotting analysis. Detailed information about the primers used to confirm the knockout strains can be found in Supplementary Data 6.

### Generation of the complementation strain

According to the established protocols[32], the complementing plasmid pFJ–$P_{Fn1529}$–*radD* was constructed in two steps as follows. First, the promoter $P_{Fn1529}$ was PCR-amplified from the genomic DNA of *F. nucleatum* ATCC 25586 by using the primers $P_{Fn1529}$–F/$P_{Fn1529}$-R, and the *radD* region encompassing the nucleotide 1 to 4,450th was PCR amplified from the gDNA of *F. nucleatum* ATCC 23726 by using the primers *radD*1–F/*radD*1–R. These two DNA fragments were then linked via overlapping PCR using the primers $P_{Fn1529}$–F/*radD1*-R while appending BamHI and PstI sites. Second, the remainder of *radD* and ~1 kb DNA fragment downstream were PCR amplified by using the primers *radD*2–F/*radD*2–Dw-R while appending PstI and XhoI sites. The generated PCR products were digested with BamHI and PstI or PstI and XhoI restriction enzymes and then ligated into the linear pUC19-catP vector.

To obtain the complementation strain Fn Δ*radD*/*radD*, the resulting plasmid pFJ–$P_{Fn1529}$–*radD* was then introduced into Fn Δ*radD* by electroporation. The complementation strain, in which the plasmid is inserted into the bacterial chromosome by homologous recombination, was selected by growing on TSPC agar plates containing 5 μg ml$^{-1}$ thiamphenicol at 37 °C under anaerobic conditions.

### Inactivation of *radD* gene in *F. nucleatum* ATCC 10953

The *radD* mutant derivative of *F. nucleatum* ATCC 10953 was generated by disrupting the *radD* encoding gene (FNP_1046) through single homologous recombination, following the method outlined previously[31,43,56]. Briefly, a 1,032 bp internal gene fragment was amplified from gDNA of *F. nucleatum* ATCC 10953 and subsequently subcloned into the linear pUC19-catP vector. The resulting plasmid, pFJ-*radD*i, was then introduced into *F. nucleatum* ATCC 10953 via electroporation and plated onto TSPC agar plates supplemented with 5 μg ml$^{-1}$ thiamphenicol. Incubation was carried out at 37 °C under anaerobic conditions.

### Structure prediction

The whole structure of the RadD protein was predicted by AlphaFold2 with Google Colab using default settings[60,61]. AlphaFold was run once with each of the five trained models; the five models generated were checked for consistency unless specified otherwise. Mean predicted local distance difference test, which indicates the accuracy of a prediction, was computed over the structure and was used for ranking the five models. We compared the top five ranked outputs and selected rank 1 to prepare the figures.

### Cell attachment assay and flow cytometry

*F. nucleatum* was inoculated into fresh TSPC medium at 1:1,000 dilution and anaerobically grown overnight to mid-log phase ($OD_{600}$ = 1.0, ~$10^9$ c.f.u. ml$^{-1}$) at 37 °C. Cell pellets, which were collected by centrifugation (5,000 × *g*, 10 min, 4 °C), were washed twice in sterile PBS and then labelled with FITC (0.1 mg ml$^{-1}$ in PBS, Yeasen Biotechnology, catalogue number 60514ES60) for 2 h at 37 °C. After three additional washes with PBS, FITC-labelled bacteria were used at a multiplicity of infection (MOI) of 50. Bacteria were co-incubated with cells grown in 12-well plates for 1 h at 37 °C in an incubator. Post incubation, the cells were subjected to two PBS washes, followed by scraping with a rubber scraper, and the cell suspension was then filtered through a 40 μm cell strainer. Flow cytometry was performed on BD LSR-Fortessa (BD Biosciences) with FACSDiva software (v.8.0.1). The acquired data were analysed using FlowJo software (v.10.4). The FACS (fluorescence-activated cell sorting) gating strategy is displayed in Supplementary Fig. 7.

### Confocal microscopy

To visualize the adhesion of *F. nucleatum* to cells, bacteria were labelled with FITC and co-incubated with HCT116 or SW480 cells that were grown to 70% confluency in 12-well plates, at 37 °C for 1 h (MOI = 50). Following two washes with PBS, the cells were fixed using 4% paraformaldehyde and then incubated with 4′,6-diamidino-2-phenylindole (DAPI). For the competition experiments, the Fn WT strain and *radD* mutant were stained with FITC and Cy3 for 2 h at 37 °C, respectively. After washing three times in PBS, FITC- and Cy3-labelled bacteria were mixed and co-incubated with cells for 1 h at 37 °C (MOI = 50). After washing twice in PBS, the cells were fixed using 4% paraformaldehyde and then incubated with DAPI.

To visualize the adhesion of *F. nucleatum* to tissues, fresh frozen tissue sections were pre-blocked with a solution of PBS supplemented with 10% goat serum for 2 h at room temperature, followed by co-incubation with FITC- or Cy3-labelled bacteria ($2.5 \times 10^7$ bacteria per ml) overnight at 4 °C. The sections were then washed once with PBS containing 0.5% Tween 20, followed by two additional washes with PBS for 10 min each. Both tumour and normal sections were prepared for each patient or mouse. For adhesion inhibition assay, bacteria were preincubated with 0.2 mg ml$^{-1}$ soluble recombinant human CD147 protein before interaction with tissues. The cells or tissue sections were then viewed under Zeiss LSM710 confocal microscope (Carl Zeiss) using ZEN 2011 software. FITC- or Cy3-labelled bacteria were counted by two

independent examiners over a total area of 4,000 μm$^2$ (each field) and converted to bacteria per square millimetre.

### TEM

For TEM analysis, cells were cultured to approximately 70% confluence in 6-well plates. Bacteria were then added for co-culture with the cells for 3 h (MOI = 50). Subsequently, the cells were washed twice with PBS and fixed in 2.5% glutaraldehyde solution. Samples were fixed with 1% osmium tetroxide, dehydrated using an ethanol and propylene oxide gradient, embedded, sectioned into 50 nm slices and stained with 3% uranyl acetate and lead citrate. The sections were then visualized using Hitachi HT7700 transmission electron microscope.

### Measurement of bacterial adhesion by fluorescence microplate reader

*F. nucleatum* was inoculated into 5 ml fresh TSPC medium and anaerobically grown overnight to an $OD_{600}$ of 1.0 (mid-log phase) at 37 °C. Subsequently, 1 ml of bacterial culture was transferred into a 1.5 ml centrifuge tube, and the pellets were collected by centrifugation (5,000 × *g*, 10 min, 4 °C). The bacteria were then washed twice with sterile PBS and re-suspended in 1 ml of FITC (0.1 mg ml$^{-1}$ in PBS) for 2 h at 37 °C. After three additional washes with PBS, 100 μl of FITC-labelled bacteria were co-incubated with cells grown in 96-well plates for 1 h at 37 °C in an incubator. After incubation, the cells were washed twice with PBS, and the fluorescence intensity of each well was measured using a fluorescent microplate reader (FLUOstar Omega, Germany).

### Measurement of bacterial invasion by plate counting

Invasion assays were conducted as previously described[20]. Cells were cultured in 12-well plates and grown to near confluency ($8 \times 10^5$). Bacteria were added at MOI = 100 and incubated under 5% $CO_2$ at 37 °C for 3 h. Following incubation, the monolayers were washed twice with PBS; 400 μl fresh medium containing metronidazole (200 μg ml$^{-1}$, Sigma, catalogue number M3761) and gentamicin (300 μg ml$^{-1}$, Sigma, catalogue number G3632) was added, and the monolayers were incubated for an additional 1 h to kill extracellular bacteria. The monolayers were washed with PBS twice before being lysed with 400 μl sterile water. The internalized bacteria were counted on TSPC agar plates after incubation for 72 h.

### Cell proliferation, migration and invasion assays

CCK-8 (Dojindo) assays and an EdU Kit (Yeasen Biotechnology, catalogue number 40276ES60) were used to evaluate cell proliferation. For the CCK-8 assay, cells were cultured in 96-well plates and exposed to bacteria (MOI = 100) or anti-CD147 antibodies (Abcam, catalogue number ab230921; dilution ratio, 1:100). Following this, 10 μl of CCK-8 solution was added, and detection and quantification were carried out as instructed by the manufacturer. When using the EdU Kit, cells were seeded in 24-well plates with 0.5 ml culture medium and incubated for 24 h. Afterwards, they were exposed to bacteria. Three hours later, the medium containing bacteria was replaced with 0.5 ml fresh medium and incubated at 37 °C for 48 h. The EdU solution was then added based on the manufacturer's instruction, and the samples were observed using a confocal microscope.

A wound-healing assay was used to examine cell migration. After exposure to bacteria for 3 h, cells were trypsinized and seeded in 12-well plates to form a confluent monolayer. A 200 μl pipette tip was used to scratch the cell monolayer in a straight line. Images were captured at 0 and 48 h post scratching, and ImageJ software (v.1.53) was used to measure the migration distance.

Transwell assays were used to test cell invasion. After co-incubation with bacteria for 3 h, cells were trypsinized and added to the upper chamber. Cells that moved across the membrane were fixed with 4% paraformaldehyde and stained with 1% crystal violet solution. Cell counts were conducted in five randomly selected fields for each chamber.

For PI3K and Wnt signalling inhibition experiment, cells were treated with LY294002 (10 μM, Yeasen Biotechnology, catalogue number 52403ES08) and IWP-2 (10 μM, Yeasen Biotechnology, catalogue number 53013ES08) respectively, for 24 h before exposure to bacteria.

### Meta-analysis of *radD* abundance in faecal samples

Meta-analysis of *radD* abundance in faecal samples from published studies was performed according to a previously published method[14]. Hits were aligned against the reference sequence and then filtered based on the percentage of sequence identity. The original sequencing data for the US and China studies are accessible from the European Nucleotide Archive with the identifiers PRJEB12449 and PRJEB10878, respectively. For the Japan study, the metadata is available from the DNA Data Bank of Japan database, identified as DRA006684. The metadata for these samples are available in Supplementary Data 1.

### Phylogenetic analysis of RadD homologues

Phylogenetic analysis of RadD homologues was performed according to a previously published method[62]. In brief, the amino acid sequences of RadD were subjected to a BLASTp (https://blast.ncbi.nlm.nih.gov/Blast.cgi) search against the database. Following this, the resulting proteins underwent alignment using the Clustal W software (v.2.1)[63]. The maximum-likelihood phylogenetic tree was generated by using the maximum-likelihood approach with the LG model and 300 bootstrap replicates in MEGA 11 program (v.11.0.11)[63]. Finally, the Newick file containing the phylogenetic tree was uploaded to the Interactive Tree of Life web server tool (https://itol.embl.de/) for further display, manipulations and annotation.

### RNA-seq

Cells were co-incubated with bacteria for 3 h at MOI = 100 for 24 h. Following PBS washes, cells were collected, and total RNA was extracted using a RNeasy Mini Kit (QIAGEN, catalogue number 74104). Subsequently, the Illumina Novaseq 6000 platform (Shanghai Genergy BioTech) was used for RNA-seq. The analytical pipeline for data processing has been outlined previously[18]. Briefly, reads were aligned to the human genome hg38 using STAR/StringTie (v.1.3.1c). The expression of the transcript was calculated by FPKM (fragments per kilobase of exon model per million mapped reads) using Perl (v.5.32.1). Differentially expressed transcripts were determined using the MA (logarithm ratio [M] versus mean average [A])-plot-based method with random sampling model in the DEGseq package (v.1.16.1) and then were further used for function and signalling pathway enrichment analysis. The RNA sequence data have been deposited in the Gene Expression Omnibus database under the accession number GSE245617.

### FISH

The FISH procedure was conducted as detailed previously[64,65]. Paraffin-embedded colon tissue sections were subjected to hybridization in a solution containing the Alexa Fluor 488-conjugated *F. nucleatum* specific probe (CGCAATACAGAGTTGAGCCCTGC) and Cy3-conjugated EUB 338 universal bacterial probe (GCTGCCTCCCGTAGGAGT). Following 24 h of incubation in a dark, humid chamber at 37 °C, the slides were rinsed with sterile double-distilled water, air-dried in the dark and mounted with DAPI anti-fade solution. Images were acquired using a Zeiss LSM710 confocal microscope (Carl Zeiss).

### Oligonucleotide transfection

The siRNAs were synthesized by Tsingke. Cells were co-transfected with siRNAs using the DharmaFECT1 siRNA transfection reagent (Dharmacon, catalogue number T-2002-03). A non-specific siRNA was used as the negative control. The sequences of siRNAs are listed in Supplementary Data 6.

### Biotin pull-down assay

Bacteria were labelled with 2 mM EZ-Link Sulfo-NHS-LC-Biotin reagent for 1 h at room temperature. After washing three times with 100 mM glycine to quench and remove excess biotin reagent, the bacteria were lysed by sonication, and membrane proteins were collected by ultracentrifugation (100,000 × *g* at 4 °C for 1 h) and re-suspended in buffer containing 40 mM n-octyl-β-D-glucopyranoside. Debris was removed from the tube by centrifugation at 4,750 × *g* for 10 min, and the supernatant was incubated with streptavidin agarose resin at 4 °C for 4 h with end-over-end mixing. Following three rounds of washing, the resin was incubated with HCT116 cell membrane proteins. Thereafter, the resin underwent three additional rounds of washing before being incubated with elution buffer. Finally, the eluted proteins were identified using mass spectrometry. The data have been deposited in the Proteomics Identifications database with the accession number PXD053279.

### Expression vectors construction and transfection

The coding sequence of *CD147*, *ITGB1* and *ANXA4* were PCR-amplified using the PrimeSTAR Max DNA Polymerase (Takara, catalogue number R045A) and then cloned into the expression vector pcDNA3.1 with *Hin*dIII and *Xba*I sites, resulting in pcDNA3.1-*CD147*, pcDNA3.1-*ITGB1* and pcDNA3.1-*ANXA4*, respectively. Subsequently, the expression vectors were transfected into HCT116 cells using FuGENE HD transfection reagent (Promega, catalogue number E2312). The primers are listed in Supplementary Data 6.

### Detection of *F. nucleatum*

Genomic DNA extraction was carried out from fresh CRC tissues using a QIAamp DNA Mini Kit (QIAGEN; catalogue number 51306) and from stool samples using a QIAamp Fast DNA Stool Mini Kit (QIAGEN, catalogue number 51604), following the manufacturer's provided protocols. qPCR was used to determine the abundance of *F. nucleatum* and the *radD* gene. The primers for each assay are listed in Supplementary Data 6.

### RNA extraction, reverse transcription and real-time PCR

Total RNA was extracted from cells or tissues using RNAiso Plus (Takara, catalogue number 9108) and reverse-transcribed using a PrimeScript RT reagent kit (Takara, catalogue number RR037A), according to the manufacturer's instructions. Each reaction contained 40 ng of complementary DNA or gDNA, and was assayed in 10 µl reactions containing 1× TB Green *Premix Ex Taq* II (Takara, catalogue number RR820A) and 0.4 µM each primer. Quantitative real-time PCR was performed in triplicate on the StepOnePlus Real-Time PCR system (Applied Biosystems, StepOne Software) under the following reaction conditions: 30 s at 95 °C, followed by 40 cycles of denaturation at 95 °C for 5 s and at 60 °C for 30 s. *GAPDH* was used as the internal reference gene for normalization of the data. All primers are listed in Supplementary Data 6.

### Western blotting

Proteins were quantified using a BCA Protein Assay Kit (Thermo Fisher Scientific, catalogue number 23225). Following this, samples were subjected to separation on SDS-PAGE and transferred onto polyvinylidene difluoride (PVDF) membranes. After blocking with 5% fat-free milk for 1 h at room temperature, the PVDF membranes were incubated with the primary antibodies overnight at 4 °C and washed three times with Tris-buffered saline–Tween 20, followed by incubation with appropriately labelled secondary antibodies for 1 h at room temperature. After washing three times with Tris-buffered saline–Tween 20, the immunoreactive proteins on the PVDF membranes were visualized using an ECL Kit (Pierce Biotechnology). Blots were visualized by ChemiDoc Imaging System using Image Lab Touch Software (Bio-Rad). Band intensities were analysed using ImageJ software. The information of all antibodies is listed in Supplementary Table 4.

### Enzyme-linked immunosorbent assay

About $5 \times 10^8$ cells were collected and washed twice with pre-cold PBS. Cells were then suspended with PBS and lysed by sonication. Debris was removed by centrifugation at 10,000 × *g* for 10 min, and the supernatant was quantified using a BCA Protein Assay Kit. Enzyme-linked immunosorbent assay kits were used to detect the concentration of PIK3R2 (Abebio, catalogue number AE27419HU), NF-κB (Abcam, catalogue number ab279874), PCNA (Abcam, catalogue number ab196270) and MMP2 (Abcam, catalogue number ab100606) following manufacturer guidelines.

### Statistical analysis

GraphPad Prism software (GraphPad, v.9.4.1) was used for the statistical analyses. Data are represented as the means ± s.e.m. Student's *t*-test was applied to compare the results between two sample groups if the data were normally distributed. One-way analysis of variance (ANOVA) was used to compare means across three groups, with multiple comparisons adjusted using either the Dunnett's or Tukey's test. If the results were skewed, comparisons were performed by the nonparametric Mann–Whitney test. Spearman correlation was used to evaluate the association. All statistical tests were two-tailed, and significance was established at $P < 0.05$.

### Reporting summary

Further information on research design is available in the Nature Portfolio Reporting Summary linked to this article.

## Data availability

Datasets analysed during the current study of the faecal metagenomic information for the United States and China studies are accessible via the European Nucleotide Archive (https://www.ebi.ac.uk/ena) with the identifiers PRJEB12449 and PRJEB10878. For the Japan study, the metadata are available via the DNA Data Bank of Japan (https://www.ddbj.nig.ac.jp/) database with accession number DRA006684. RNA-seq data from this study have been deposited in the Gene Expression Omnibus (https://www.ncbi.nlm.nih.gov/geo/) database under the accession number GSE245617. Mass spectrometry data have been deposited in the Proteomics Identifications (PRIDE; https://www.ebi.ac.uk/pride/) database under the accession number PXD053279. Source data are provided with this paper.

## References

1. Siegel, R. L., Wagle, N. S., Cercek, A., Smith, R. A. & Jemal, A. Colorectal cancer statistics, 2023. *CA Cancer J. Clin.* **73**, 233–254 (2023).
2. Morgan, E. et al. Global burden of colorectal cancer in 2020 and 2040: incidence and mortality estimates from GLOBOCAN. *Gut* **72**, 338–344 (2022).
3. Nougayrede, J. P. et al. *Escherichia coli* induces DNA double-strand breaks in eukaryotic cells. *Science* **313**, 848–851 (2006).
4. Wu, S. G. et al. A human colonic commensal promotes colon tumorigenesis via activation of T helper type 17 T cell responses. *Nat. Med.* **15**, 1016–U1064 (2009).
5. Tsoi, H. et al. *Peptostreptococcus anaerobius* induces intracellular cholesterol biosynthesis in colon cells to induce proliferation and causes dysplasia in mice. *Gastroenterology* **152**, 1419–1433 (2017).
6. Wilson et al. The human gut bacterial genotoxin colibactin alkylates DNA. *Science* **363**, eaar 7785 (2019).
7. Goodwin, A. C. et al. Polyamine catabolism contributes to enterotoxigenic *Bacteroides fragilis*-induced colon tumorigenesis. *Proc. Natl Acad. Sci. USA* **108**, 15354–15359 (2011).
8. Long, X. H. et al. *Peptostreptococcus anaerobius* promotes colorectal carcinogenesis and modulates tumour immunity. *Nat. Microbiol.* **4**, 2319–2330 (2019).

9. Kostic, A. D. et al. Genomic analysis identifies association of *Fusobacterium* with colorectal carcinoma. *Genome Res.* **22**, 292–298 (2012).
10. Castellarin, M. et al. *Fusobacterium nucleatum* infection is prevalent in human colorectal carcinoma. *Genome Res.* **22**, 299–306 (2012).
11. Dai, Z. W. et al. Multi-cohort analysis of colorectal cancer metagenome identified altered bacteria across populations and universal bacterial markers. *Microbiome* **6**, 70 (2018).
12. Thomas, A. M. et al. Metagenomic analysis of colorectal cancer datasets identifies cross-cohort microbial diagnostic signatures and a link with choline degradation. *Nat. Med.* **25**, 667–678 (2019).
13. Al-Hassi, H. O., Ng, O. & Brookes, M. Tumour-associated and non-tumour-associated microbiota in colorectal cancer. *Gut* **67**, 395 (2018).
14. Wirbel, J. et al. Meta-analysis of fecal metagenomes reveals global microbial signatures that are specific for colorectal cancer. *Nat. Med.* **25**, 679–689 (2019).
15. Yachida, S. et al. Metagenomic and metabolomic analyses reveal distinct stage-specific phenotypes of the gut microbiota in colorectal cancer. *Nat. Med.* **25**, 968–976 (2019).
16. Okuda, S. et al. Profiling of host genetic alterations and intra-tumor microbiomes in colorectal cancer. *Comput. Struct. Biotechnol. J.* **19**, 3330–3338 (2021).
17. Mima, K. et al. *Fusobacterium nucleatum* in colorectal carcinoma tissue and patient prognosis. *Gut* **65**, 1973–1980 (2016).
18. Yu, T. et al. *Fusobacterium nucleatum* promotes chemoresistance to colorectal cancer by modulating autophagy. *Cell* **170**, 548–563.e516 (2017).
19. Yamamoto, S. et al. Heterogeneous distribution of *Fusobacterium nucleatum* in the progression of colorectal cancer. *J. Gastroenterol. Hepatol.* **36**, 1869–1876 (2021).
20. Brennan, C. A. & Garrett, W. S. *Fusobacterium nucleatum*-symbiont, opportunist and oncobacterium. *Nat. Rev. Microbiol.* **17**, 156–166 (2019).
21. Rubinstein, M. R. et al. *Fusobacterium nucleatum* promotes colorectal carcinogenesis by modulating E-cadherin/β-catenin signaling via its FadA adhesin. *Cell Host Microbe* **14**, 195–206 (2013).
22. Rubinstein, M. R. et al. *Fusobacterium nucleatum* promotes colorectal cancer by inducing Wnt/β-catenin modulator Annexin A1. *EMBO Rep.* **20**, e47638 (2019).
23. Zhang, Y. et al. *Fusobacterium nucleatum* promotes colorectal cancer cells adhesion to endothelial cells and facilitates extravasation and metastasis by inducing ALPK1/NF-κB/ICAM1 axis. *Gut Microbes* **14**, 2038852 (2022).
24. Guo, P. et al. FadA promotes DNA damage and progression of *Fusobacterium nucleatum*-induced colorectal cancer through up-regulation of chk2. *J. Exp. Clin. Cancer Res.* **39**, 202 (2020).
25. Ikegami, A., Chung, P. & Han, Y. P. W. Complementation of the *fadA* mutation in *Fusobacterium nucleatum* demonstrates that the surface-exposed adhesin promotes cellular invasion and placental colonization. *Infect. Immun.* **77**, 3075–3079 (2009).
26. Xu, M. H. et al. FadA from *Fusobacterium nucleatum* utilizes both secreted and nonsecreted forms for functional oligomerization for attachment and invasion of host cells. *J. Biol. Chem.* **282**, 25000–25009 (2007).
27. Abed, J. et al. Fap2 mediates *Fusobacterium nucleatum* colorectal adenocarcinoma enrichment by binding to tumor-expressed Gal-GalNAc. *Cell Host Microbe* **20**, 215–225 (2016).
28. Casasanta, M. A. et al. *Fusobacterium nucleatum* host-cell binding and invasion induces IL-8 and CXCL1 secretion that drives colorectal cancer cell migration. *Sci. Signal.* **13**, eaba9157 (2020).
29. Takemoto, T. et al. Purification of arginine-sensitive hemagglutinin from *Fusobacterium nucleatum* and its role in coaggregation. *J. Periodontal Res.* **28**, 21–26 (1993).
30. Edwards, A. M. et al. Association of a high-molecular weight arginine-binding protein of *Fusobacterium nucleatum* ATCC 10953 with adhesion to secretory immunoglobulin A and coaggregation with *Streptococcus cristatus*. *Oral Microbiol. Immunol.* **22**, 217–224 (2007).
31. Kaplan, C. W., Lux, R., Haake, S. K. & Shi, W. Y. The outer membrane protein RadD is an arginine-inhibitable adhesin required for inter-species adherence and the structured architecture of multispecies biofilm. *Mol. Microbiol.* **71**, 35–47 (2009).
32. Wu, C. G. et al. Genetic and molecular determinants of polymicrobial interactions in *Fusobacterium nucleatum*. *Proc. Natl Acad. Sci. USA* **118**, e2006482118 (2021).
33. Kaplan, C. W. et al. Outer membrane proteins Fap2 and RadD induce cell death in human lymphocytes. *Infect. Immun.* **78**, 4773–4778 (2010).
34. Vogtmann, E. et al. Colorectal cancer and the human gut microbiome: reproducibility with whole-genome shotgun sequencing. *PLoS ONE* **11**, e0155362 (2016).
35. Yu, J. et al. Metagenomic analysis of faecal microbiome as a tool towards targeted non-invasive biomarkers for colorectal cancer. *Gut* **66**, 70–78 (2017).
36. Asgari, R. et al. CD147 and MMPs as key factors in physiological and pathological processes. *Biomed. Pharmacother.* **157**, 113983 (2023).
37. Huang, Y., Xu, J., Xu, Y., Li, L. & Zheng, M. CD147 promotes glucose metabolism, invasion and metastasis via PI3K/AKT pathway in oral squamous cell carcinomas. *Transl. Cancer Res.* **8**, 1486–1496 (2019).
38. Cheng, C. Y., Hsieh, H. L., Hsiao, L. D. & Yang, C. M. PI3K/Akt/JNK/NF-κB is essential for MMP-9 expression and outgrowth in human limbal epithelial cells on intact amniotic membrane. *Stem Cell Res.* **9**, 9–23 (2012).
39. McCoy, A. N. et al. *Fusobacterium* is associated with colorectal adenomas. *PLoS ONE* **8**, e53653 (2013).
40. Feng, Q. et al. Gut microbiome development along the colorectal adenoma-carcinoma sequence. *Nat. Commun.* **6**, 6528 (2015).
41. Li, Y. Y. et al. Association of *Fusobacterium nucleatum* infection with colorectal cancer in Chinese patients. *World J. Gastroenterol.* **22**, 3227–3233 (2016).
42. He, X. et al. Adherence to streptococci facilitates *Fusobacterium nucleatum* integration into an oral microbial community. *Microb. Ecol.* **63**, 532–542 (2012).
43. Guo, L., Shokeen, B., He, X., Shi, W. & Lux, R. *Streptococcus mutans* SpaP binds to RadD of *Fusobacterium nucleatum* ssp. *polymorphum*. *Mol. Oral. Microbiol.* **32**, 355–364 (2017).
44. Cisar, J. O., Kolenbrander, P. E. & Mcintire, F. C. Specificity of coaggregation reactions between human oral *Streptococci* and strains of *Actinomyces viscosus* or *Actinomyces naeslundii*. *Infect. Immun.* **24**, 742–752 (1979).
45. Engevik, M. A. et al. *Fusobacterium nucleatum* adheres to *Clostridioides difficile* via the RadD adhesin to enhance biofilm formation in intestinal mucus. *Gastroenterology* **160**, 1301–1314.e8 (2021).
46. Lima, B. P., Hu, L. I., Vreeman, G. W., Weibel, D. B. & Lux, R. The oral bacterium *Fusobacterium nucleatum* binds *Staphylococcus aureus* and alters expression of the staphylococcal accessory regulator *sarA*. *Microb. Ecol.* **78**, 336–347 (2019).
47. Wu, T. et al. Cellular components mediating coadherence of *Candida albicans* and *Fusobacterium nucleatum*. *J. Dent. Res.* **94**, 1432–1438 (2015).
48. Bor, B., Cen, L., Agnello, M., Shi, W. & He, X. Morphological and physiological changes induced by contact-dependent interaction between *Candida albicans* and *Fusobacterium nucleatum*. *Sci. Rep.* **6**, 27956 (2016).

49. Park, J., Shokeen, B., Haake, S. K. & Lux, R. Characterization of *Fusobacterium nucleatum* ATCC 23726 adhesins involved in strain-specific attachment to *Porphyromonas gingivalis*. *Int. J. Oral. Sci.* **8**, 138–144 (2016).
50. Dhanda, A. S., Yu, C. & Guttman, J. A. Distribution of CD147 during *Enteropathogenic Escherichia coli* and *Salmonella enterica* Serovar Typhimurium infections. *Anat. Rec.* **302**, 2224–2232 (2019).
51. Till, A. et al. A role for membrane-bound CD147 in NOD2-mediated recognition of bacterial cytoinvasion. *J. Cell Sci.* **121**, 487–495 (2008).
52. Bernard, S. C. et al. Pathogenic *Neisseria meningitidis* utilizes CD147 for vascular colonization. *Nat. Med.* **20**, 725–731 (2014).
53. Tito, R. Y. et al. Microbiome confounders and quantitative profiling challenge predicted microbial targets in colorectal cancer development. *Nat. Med.* **30**, 1339–1348 (2024).
54. Zepeda-Rivera, M. et al. A distinct *Fusobacterium nucleatum* clade dominates the colorectal cancer niche. *Nature* **628**, 424–432 (2024).
55. Wu, C. G. et al. Forward genetic dissection of biofilm development by *Fusobacterium nucleatum*: novel functions of cell division proteins FtsX and EnvC. *mBio* **9**, e00360-18 (2018).
56. Haake, S. K., Yoder, S. & Gerardo, S. H. Efficient gene transfer and targeted mutagenesis in *Fusobacterium nucleatum*. *Plasmid* **55**, 27–38 (2006).
57. Lampe, D. J., Akerley, B. J., Rubin, E. J., Mekalanos, J. J. & Robertson, H. M. Hyperactive transposase mutants of the *Himar1* mariner transposon. *Proc. Natl Acad. Sci. USA* **96**, 11428–11433 (1999).
58. Cartman, S. T. & Minton, N. P. A mariner-based transposon system for in vivo random mutagenesis of *Clostridium difficile*. *Appl. Environ. Microbiol.* **76**, 1103–1109 (2010).
59. Zhang, Y. et al. Development of an inducible transposon system for efficient random mutagenesis in *Clostridium acetobutylicum*. *FEMS Microbiol. Lett.* **363**, fnw065 (2016).
60. Jumper, J. et al. Highly accurate protein structure prediction with AlphaFold. *Nature* **596**, 583–589 (2021).
61. Fontana, P. et al. Structure of cytoplasmic ring of nuclear pore complex by integrative cryo-EM and AlphaFold. *Science* **376**, eabm9326 (2022).
62. Yang, G. H. et al. Discovery of an ene-reductase for initiating flavone and flavonol catabolism in gut bacteria. *Nat. Commun.* **12**, 790 (2021).
63. Larkin, M. A. et al. Clustal W and clustal X version 2.0. *Bioinformatics* **23**, 2947–2948 (2007).
64. Kostic, A. D. et al. *Fusobacterium nucleatum* potentiates intestinal tumorigenesis and modulates the tumor-immune microenvironment. *Cell Host Microbe* **14**, 207–215 (2013).
65. Bullman, S. et al. Analysis of *Fusobacterium* persistence and antibiotic response in colorectal cancer. *Science* **358**, 1443–1448 (2017).


## Acknowledgements

We thank all patients and individuals for their participation in our study. This study was supported by grants from the National Key R&D Program of China (2020YFA0509200), National Natural Science Foundation of China (82250005, 82330086, 81830081, 32100138, 82203227), Project of the State Key Laboratory of Oncogenes and Related Genes (KF2128-93), Shanghai Municipal Health Commission, Collaborative Innovation Cluster Project (2019CXJQ02), Clinical Research Plan of Shanghai Hospital Development Center (SHDC2020CR1034B), the Shanghai Science and Technology Commission (20JC1410100), Innovative Research Team of High-level Local Universities in Shanghai (SHSMU-ZDCX2021030) and China Postdoctoral Science Foundation (2022M712128).

## Author contributions

L.Z., X.-X.L. and J.-Y.F. conceived the project; L.Z. and X.-X.L. were responsible for designing and conducting experiments, analysed data, and drafting the manuscript; J.Q. provided structure prediction of the RadD protein using AlphaFold2. Z.-H.T. and J.-X.H. supplied *Apc*$^{Min/+}$ mice for breeding; Z.-Y.Z. provided a portion of tissue samples from patients with CRC in cohort 3; Y.C. and X.C. helped with pathological diagnosis; N.W., Y.R., Y.-L.X., S.-S.J., J.-L.L., H.C., C.-B.Z., Z.W., Z.-Z.Z., J.H., H.-Y.C., W.J., Y.-X.C., X.Z. and J.Y. provided fruitful discussions; J.-Y.F. acquired the funding; L.Z., X.-X.L. and J.-Y.F. supervised the study; L.Z., X.-X.L. and J.-Y.F. collaborated in revising the draft, incorporating input from all authors.

## Competing interests

The authors declare no competing interests.

## Additional information

**Extended data** is available for this paper at https://doi.org/10.1038/s41564-024-01784-w.

**Supplementary information** The online version contains supplementary material available at https://doi.org/10.1038/s41564-024-01784-w.

**Correspondence and requests for materials** should be addressed to Jing-Yuan Fang.

**Peer review information** *Nature Microbiology* thanks Tracy Lee, Elisabeth Letellier and the other, anonymous, reviewer(s) for their contribution to the peer review of this work.

https://doi.org/10.1038/s41564-024-01784-w

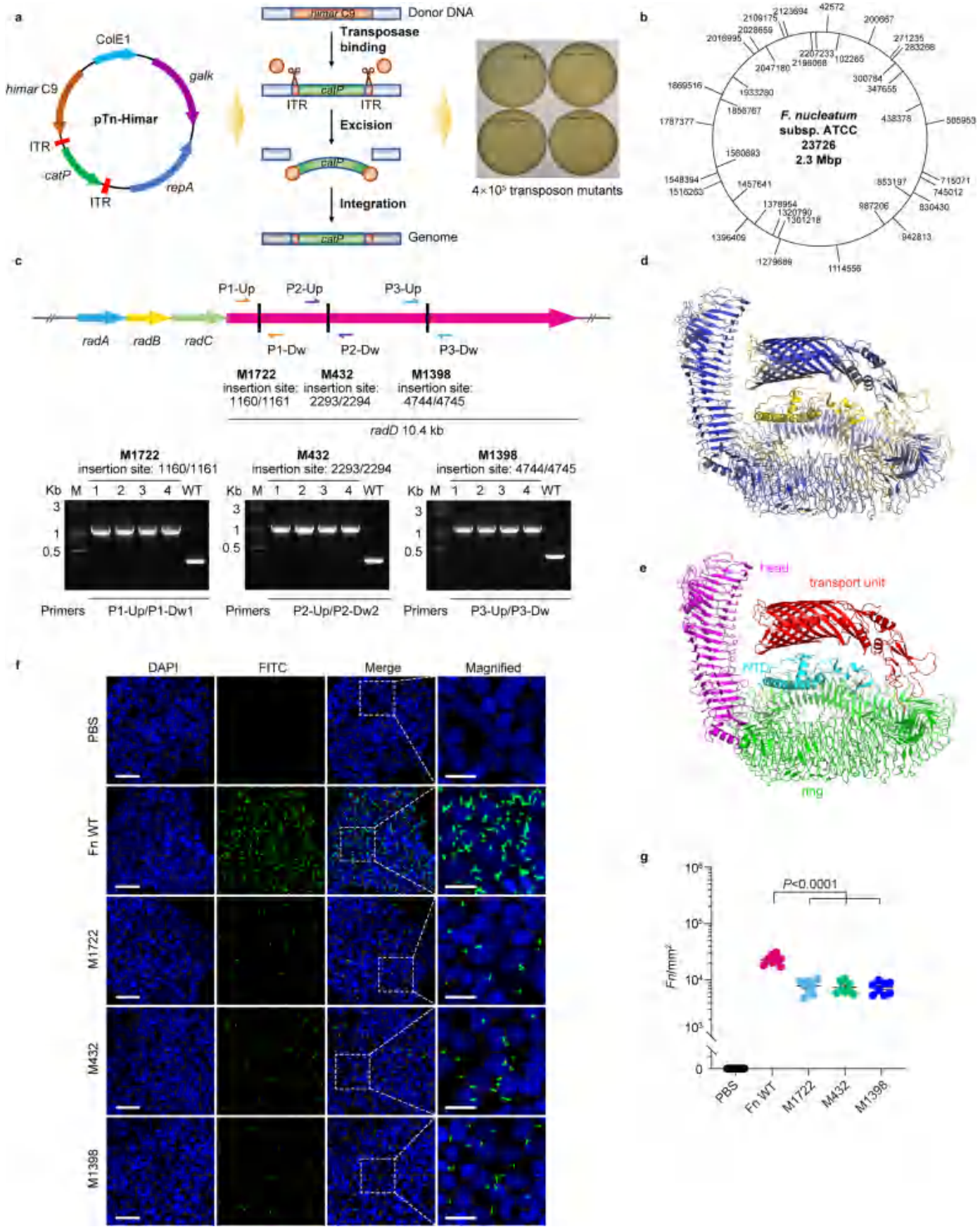


**Extended Data Fig. 1 | See next page for caption.**

https://doi.org/10.1038/s41564-024-01784-w

**Extended Data Fig. 1 | Illustration of constructing a transposon mutagenesis library and identified *radD* gene was necessary for *F. nucleatum* attachment to HCT116 cells. a**, The mariner plasmids pTn-Himar1 was transferred into *F. nucleatum* to construct a whole-genome transposon insertion collection. **b**, Genetic map of mariner transposon insertions. A total of forty independent transposon insertions were sequenced. Insertions in the plus orientation are indicated on the outer circle, while insertions in the minus orientation are marked on the inner circle. Numeric values represent the exact insertion points based on the genome sequence data for *F. nucleatum* ATCC 23726 (Refseq number GCF_003019785.1; GenBank accession number GCA_003019785.1). **c**, PCR verification of the transposon location in three *radD* insertion mutants (M1722, insertion site: 1160/1161; M432, insertion site: 2293/2294; M1398, insertion site: 4744/4745). The lower figure displays gel electrophoresis results of PCR products obtained from four colonies, randomly selected from each of the three *radD* insertion mutants. M: DNA marker; WT: *F. nucleatum* wild-type strain. **d**, The confidence of predicated structure of RadD. The structure is displayed as a cartoon and colored by pLDDT (predicted local distance difference test), blue, high confidence; yellow, medial confidence; red, low confidence. **e**, Overall predicated structure of RadD. The structure is shown as a cartoon and colored by domains, cyan, NTD (N-terminal domain); magentas, head; green, ring; red, transport unit. **f**, Representative confocal images of FITC-labeled (green) M1722, M432 and M1398 attachment to DAPI-stained (blue) HCT116 cells. Scale bars, 50 μm (left panels) and 20 μm (magnified images). **g**, Quantitation of *F. nucleatum* binding performed in f (n = 8 biological replicates). Data are presented as the mean ± SEM from three independent experiments. *P* values were determined by Brown–Forsythe and Welch ANOVA test with Dunnett's test (**g**).

https://doi.org/10.1038/s41564-024-01784-w

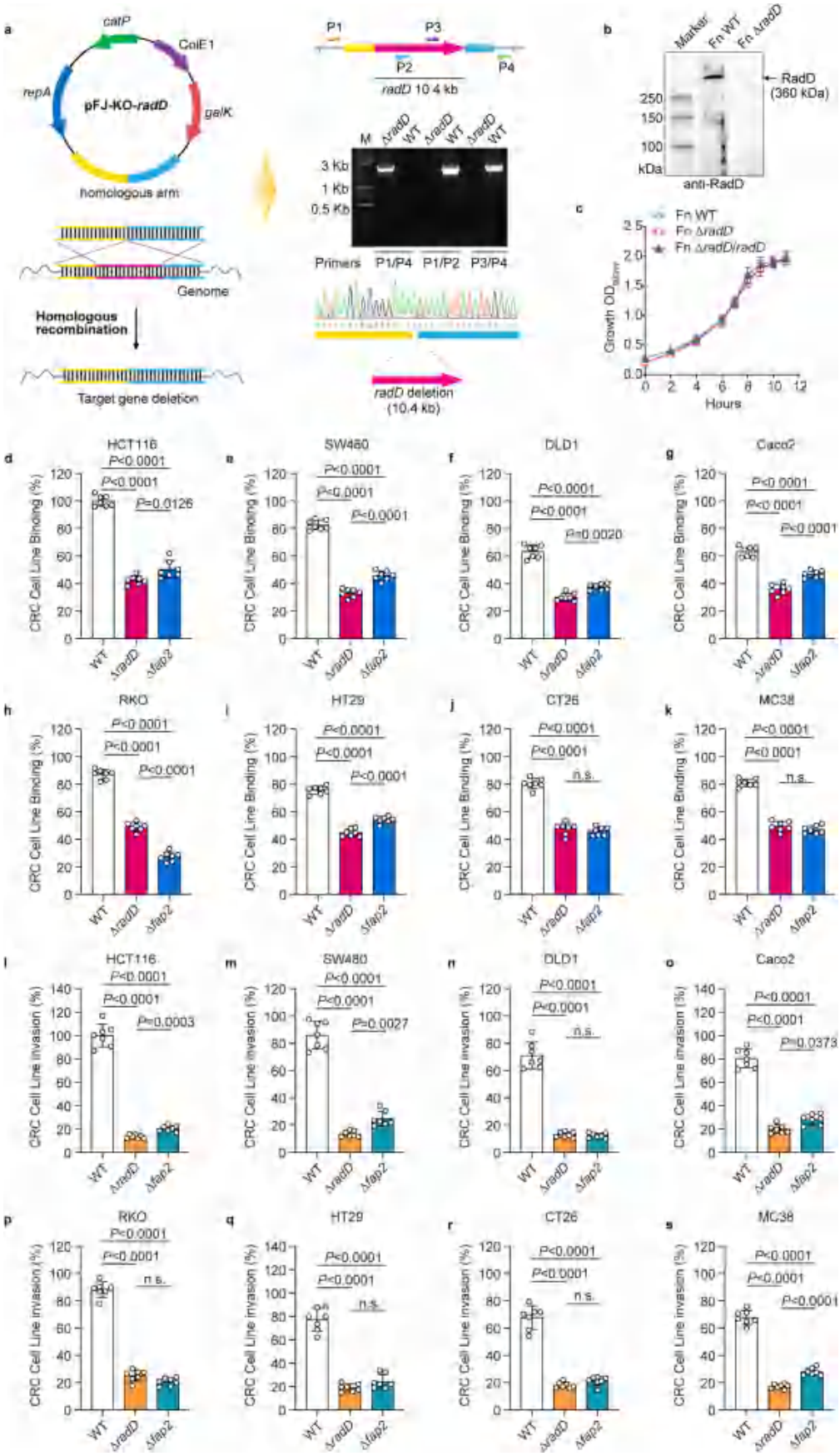


**Extended Data Fig. 2 | See next page for caption.**

https://doi.org/10.1038/s41564-024-01784-w

**Extended Data Fig. 2 | *radD*-deletion strain Fn Δ*radD* was constructed in *F. nucleatum*, and it was defective for attachment and invasion, compared to wild-type strain. a**, Schematic for the generation of Fn Δ*radD* by homologous recombination and PCR was performed to confirm *radD* gene was knockout. **b**, Western blot was carried out to validate the mutant. Three independent experiments were repeated showing the similar results. **c**, Validation that Fn Δ*radD* grew the same as Fn WT and Fn Δ*radD/radD*. n = 3 biological replicates in each group. **d**–**k**, The relative level of attachment of Fn Δ*radD*, Fn Δ*fap2* and Fn WT to human CRC cell lines HCT116 (**d**), SW480 (**e**), DLD1 (**f**), Caco2 (**g**), RKO (**h**), HT29 (**i**), and mouse CRC cell lines CT26 (**j**) and MC38 (**k**). n = 7 biological replicates in each group. **l**–**s**, The relative level of invasion of Fn Δ*radD*, Fn Δ*fap2* and Fn WT to human CRC cell lines HCT116 (**l**), SW480 (**m**), DLD1 (**n**), Caco2 (**o**), RKO (**p**), HT29 (**q**), and mouse CRC cell lines CT26 (**r**) and MC38 (**s**). n = 7 biological replicates in each group. Data are presented as the mean ± SEM from three independent experiments. *P* values were calculated using one-way ANOVA with Turkey's test (**d**-**k** and **o**-**s**) or Brown–Forsythe and Welch ANOVA test with Dunnett's test (**l**-**n**).

https://doi.org/10.1038/s41564-024-01784-w

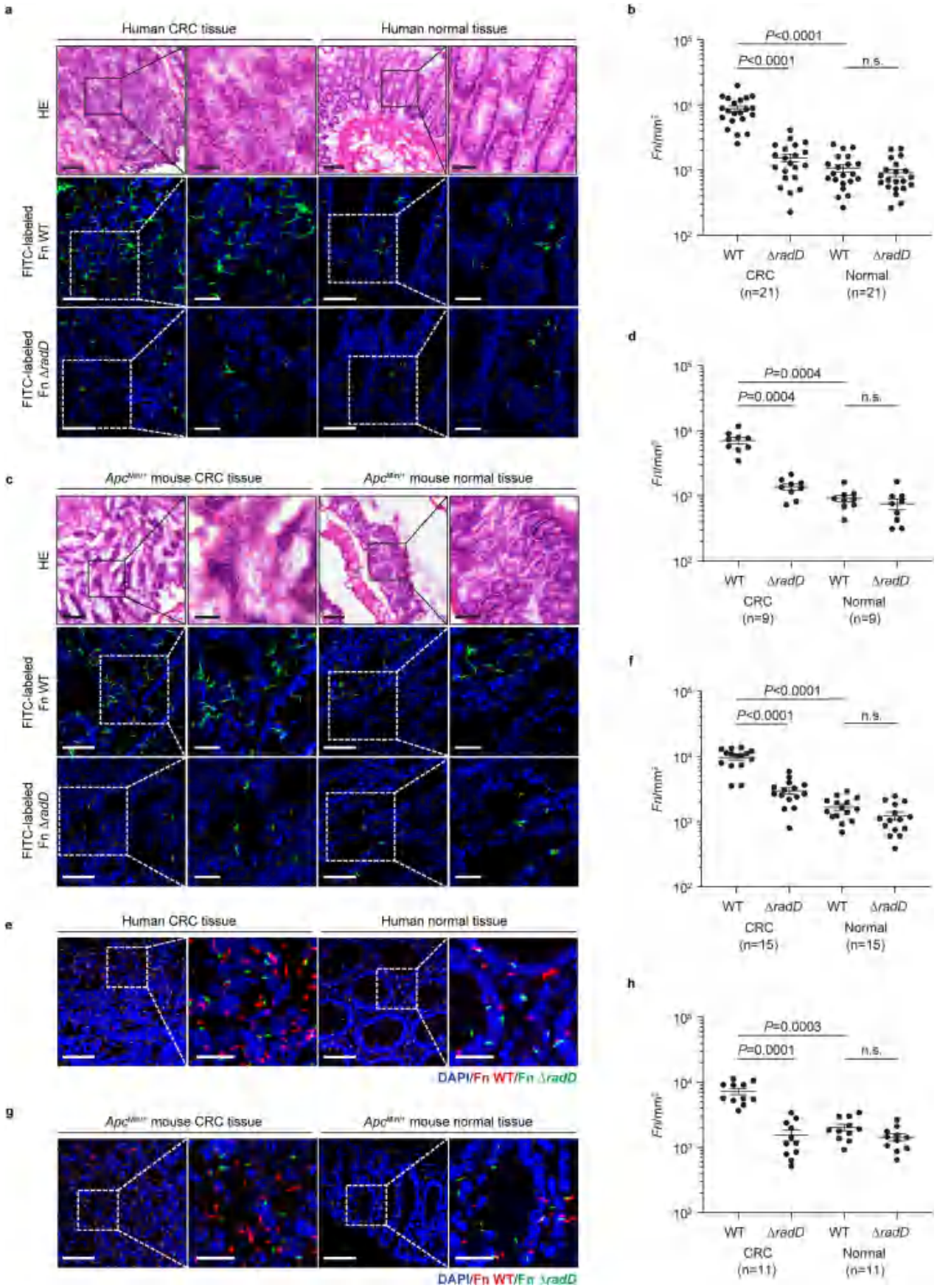


**Extended Data Fig. 3 | See next page for caption.**

https://doi.org/10.1038/s41564-024-01784-w

**Extended Data Fig. 3 | RadD mediates adhesion of *F. nucleatum* to human and mouse CRC tissues. a**, Binding of FITC-labeled Fn WT and Fn Δ*radD* to DAPI-stained human CRC and normal tissues. Scale bars in hematoxylin-eosin (HE) stained sections, 150 µm (left panels) and 50 µm (magnified images); scale bars in confocal images, 50 µm (left panels) and 20 µm (magnified images). **b**, Quantitation of *F. nucleatum* binding performed in **a** (n = 21 independent samples). **c**, Binding of FITC-labeled Fn WT and Fn Δ*radD* to DAPI-stained $Apc^{Min/+}$ mouse CRC and normal tissues. Scale bars in HE stained sections, 150 µm (left panels) and 50 µm (magnified images); scale bars in confocal images, 50 µm (left panels) and 20 µm (magnified images). **d**, Quantitation of *F. nucleatum* binding performed in **c** (n = 9 independent samples). **e**, Representative confocal images of FITC-labeled Fn Δ*radD* (green) and Cy3-labled Fn WT (red) binding to DAPI-stained (blue) human CRC and normal tissues. Scale bars, 50 µm (left panels) and 20 µm (magnified images). **f**, Quantitation of *F. nucleatum* binding performed in **e** (n = 15 independent samples). **g**, Representative confocal images of FITC-labeled Fn Δ*radD* (green) and Cy3-labled Fn WT (red) binding to DAPI-stained (blue) $Apc^{Min/+}$ mouse CRC and normal tissues. Scale bars, 50 µm (left panels) and 20 µm (magnified images). **h**, Quantitation of *F. nucleatum* binding performed in **g** (n = 11 independent samples). Data are presented as mean ± SEM. *P* values were determined by Brown–Forsythe and Welch ANOVA test with Dunnett's test (**b**, **d**, **f** and **h**).

https://doi.org/10.1038/s41564-024-01784-w

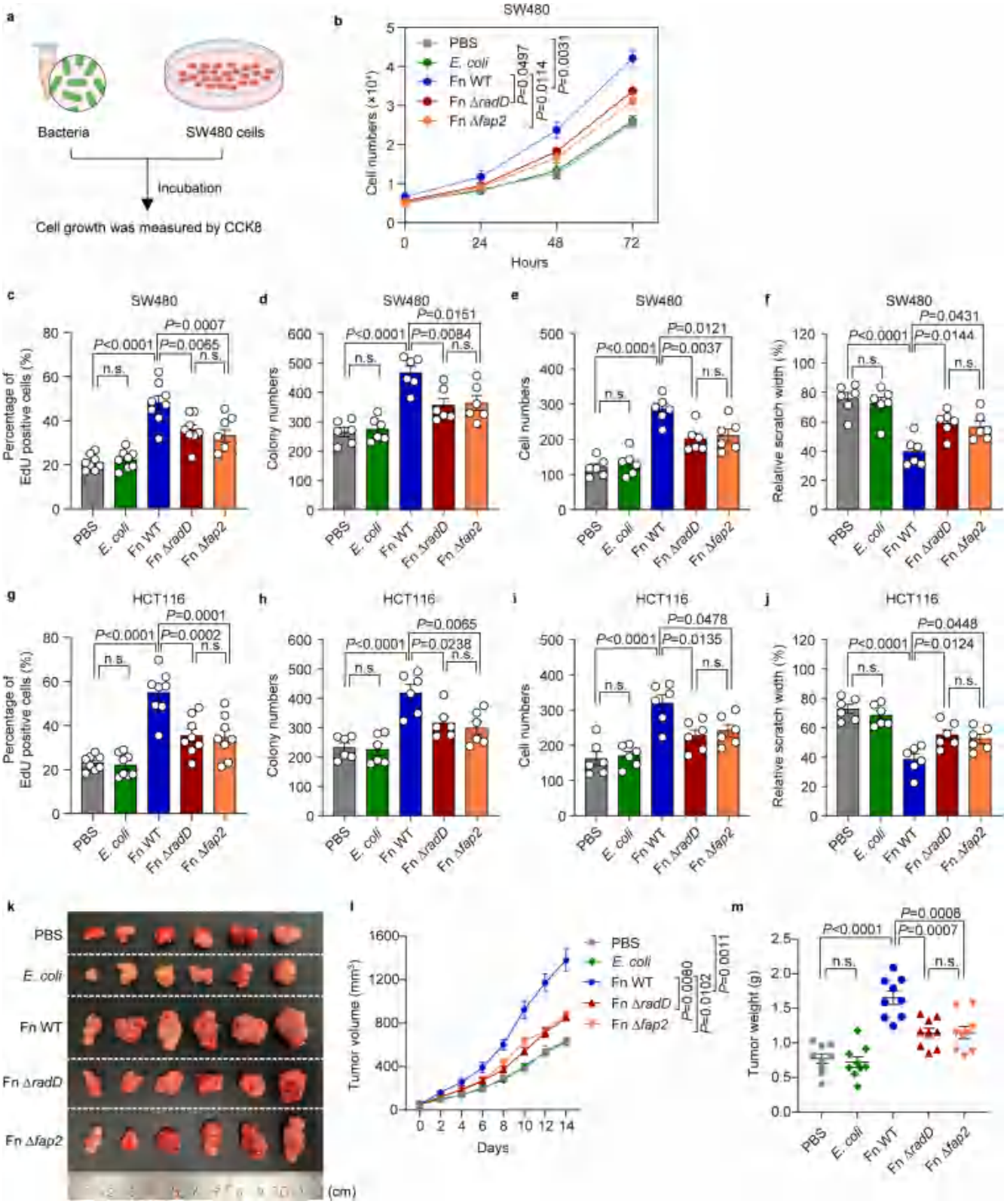


**Extended Data Fig. 4 | See next page for caption.**

https://doi.org/10.1038/s41564-024-01784-w

**Extended Data Fig. 4 | *F. nucleatum* RadD induced cell proliferation, migration and invasion *in vitro*, and promoted the tumor growth *in vivo*.** **a**, SW480 cell proliferation was determined by CCK-8 assay. **b**, Fn WT stimulated proliferation of human CRC cell lines SW480, compared to those treated with PBS or incubated with *E. coli*. Fn Δ*radD* and Fn Δ*fap2* only weakly stimulated their growth. n = 3 biological replicates in each group. **c** and **g**, Quantitation of the percentages of EdU-positive SW480 cells (**c**) or HCT116 cells (**g**) are shown (n = 8 biological replicates). **d** and **h**, Colony-forming efficiency assay of SW480 cells (**d**) or HCT116 cells (**h**) (n = 6 biological replicates). **e** and **i**, Quantitative analysis of SW480 cells (**e**) and HCT116 cells (**i**) invasion using Transwell assays (n = 6 biological replicates). **f** and **j**, Quantitative analysis of SW480 cells (**f**) and HCT116 cells (**j**) migration by scratch assays (n = 6 biological replicates). **k**, Images of representative SW480 subcutaneous tumors after the intra-tumoral injection of the indicated bacteria in BALB/c nude mice. **l** and **m**, The tumor volume ($mm^3$) (**l**) and weight (**g**) (**m**) were measured and shown (n = 9 mice per group). Data are presented as mean ± SEM from three independent experiments. *P* values were determined by two-way ANOVA with Turkey's test (**b** and **l**) and one-way ANOVA with Turkey's test (**c**–**j** and **m**). Scheme in panel **a** was partially created with BioRender.com.

https://doi.org/10.1038/s41564-024-01784-w

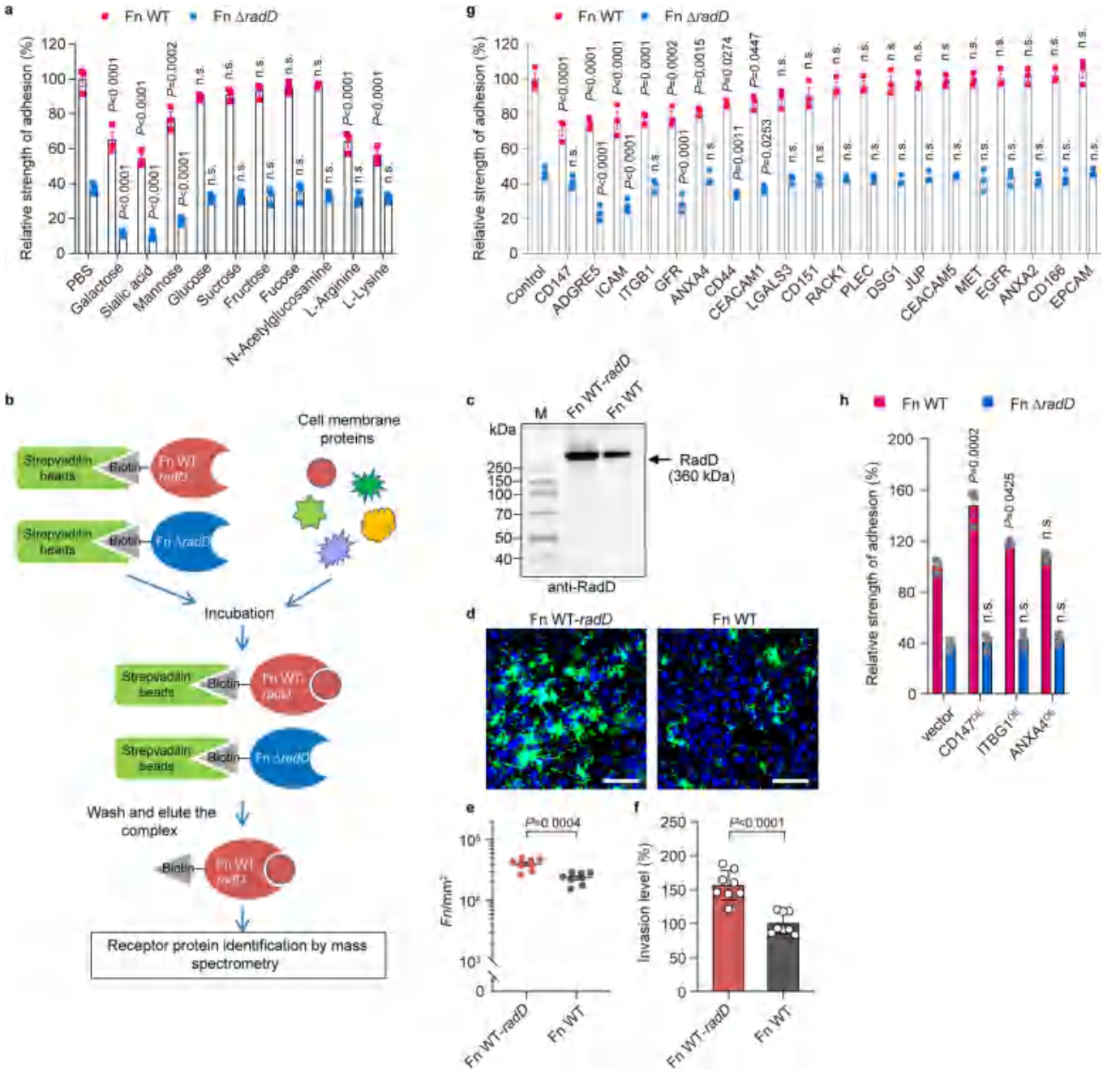


**Extended Data Fig. 5 | A Combined genetics and proteomics approach demonstrated that CD147 is a potent binding partner for *F. nucleatum* RadD. a**, Various sugars (200 mM), L-Arginine or L-Lysine (50 mM) were added to HCT116 cells prior to the addition of Fn WT or Fn Δ*radD*. The attachment level was quantified as a percentage relative to the control group. n = 3 biological replicates in each group. **b**, Biotin pull-down assay was performed to identify the corresponding host receptor for *F. nucleatum* RadD. The overexpression strain Fn WT-*radD* and knockout strain Fn Δ*radD* were labeled with biotin. Bacteria lysed by sonication, membrane proteins collected via ultracentrifugation, and then incubated with streptavidin agarose resin with end-over-end mixing, followed by overnight incubation with HCT116 cell membrane proteins at 4°C. Eluted proteins were identified using mass spectrometry. **c**, The expression levels of RadD protein in Fn WT-*radD* and Fn WT were assessed by western blot. Three independent experiments were repeated showing the similar results. **d**, Representative confocal images of FITC-labeled (green) Fn WT-*radD* and Fn WT attachment to DAPI-stained (blue) HCT116 cells. Scale bars, 50 μm. **e**, Quantitation of *F. nucleatum* binding performed in **d** (n = 8 biological replicates). **f**, The relative level of invasion of Fn WT-*radD* and Fn WT to HCT116 cells (n = 8 biological replicates). **g**, The relative levels of attachment of Fn WT and Fn Δ*radD* to HCT116 cells which either transfected with target-specific siRNAs or control siRNA. n = 3 biological replicates in each group. **h**, The relative levels of attachment of Fn WT and Fn Δ*radD* to HCT116 cells overexpressing CD147, ITGB1 or ANXA4 (n = 3 biological replicates). Data are presented as mean ± SEM from three independent experiments. *P* values were determined by one-way ANOVA with Dunnett's test (**a**, **g**–**h**) and unpaired two-tailed Student's *t*-test (**e** and **f**).

https://doi.org/10.1038/s41564-024-01784-w

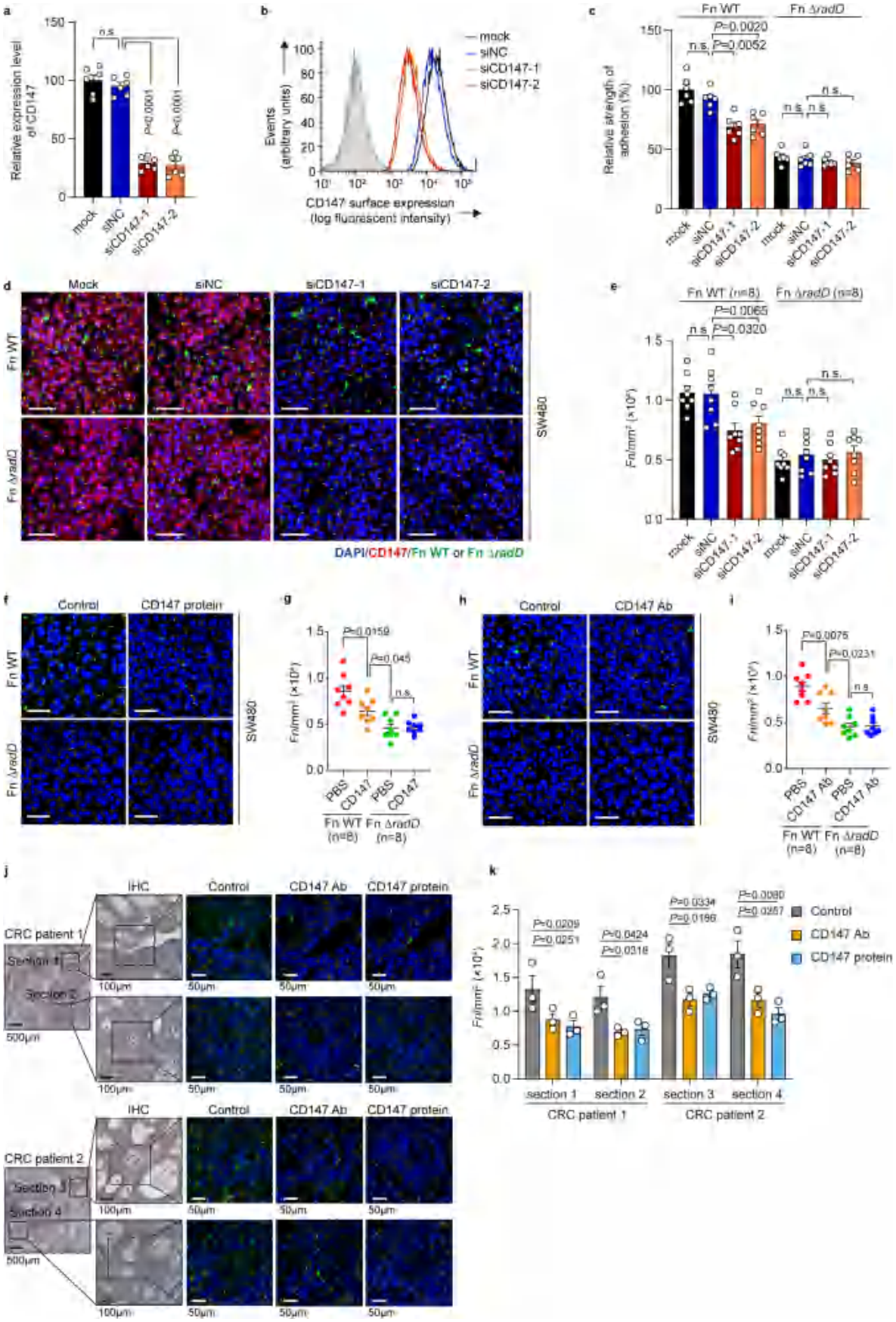


**Extended Data Fig. 6 | See next page for caption.**

https://doi.org/10.1038/s41564-024-01784-w

**Extended Data Fig. 6 | *F. nucleatum* RadD binding to CRC cells or tissues by interacting with cell surface receptor CD147. a**, The relative expression levels of CD147 in SW480 cells after transfection with either siCD147-1 or siCD147-2 (n = 6 biological replicates). siNC serves as the negative control. **b**, FACS analysis of CD147 expression in SW480 cells, with siNC as a negative control. Three independent experiments were repeated showing the similar results. **c**, Adhesion of Fn WT and Fn Δ*radD* to CD147-depleted (siCD147-1 and siCD147-2) or control (siNC) SW480 cells (n = 6 biological replicates). **d**, Immunofluorescence analysis of FITC-labeled Fn WT and Fn Δ*radD* attachment to CD147-depleted (siCD147-1 and siCD147-2) or control (siNC) SW480 cells. Scale bars, 50 μm. **e**, Quantitation of *F. nucleatum* binding performed in **d** (n = 8 biological replicates). **f** and **g**, Representative images (**f**) and quantitation (**g**) of FITC-labeled (green) Fn WT and Fn Δ*radD* attachment to DAPI-stained (blue) SW480 cells preincubated with soluble CD147 proteins (n = 8 biological replicates). Scale bars, 50 μm. **h** and **i**, Representative images (**h**) and quantitation (**i**) of FITC-labeled (green) Fn WT and Fn Δ*radD* attachment to DAPI-stained (blue) SW480 cells preincubated with anti-CD147 antibodies (n = 8 biological replicates). Scale bars, 50 μm. **j**, Representative images of FITC-labeled (green) Fn WT and Fn Δ*radD* attachment to DAPI-stained (blue) colonic tissues from two CRC patients preincubated with soluble CD147 proteins or anti-CD147 antibodies. PBS was used for negative control. **k**, Quantitation of *F. nucleatum* binding in **j** (n = 3 independent area of each section). Data are presented as mean ± SEM from three independent experiments. *P* values were determined by one-way ANOVA with Turkey's test (**g** and **i**) or Dunnett's test (**c, e** and **k**).

https://doi.org/10.1038/s41564-024-01784-w

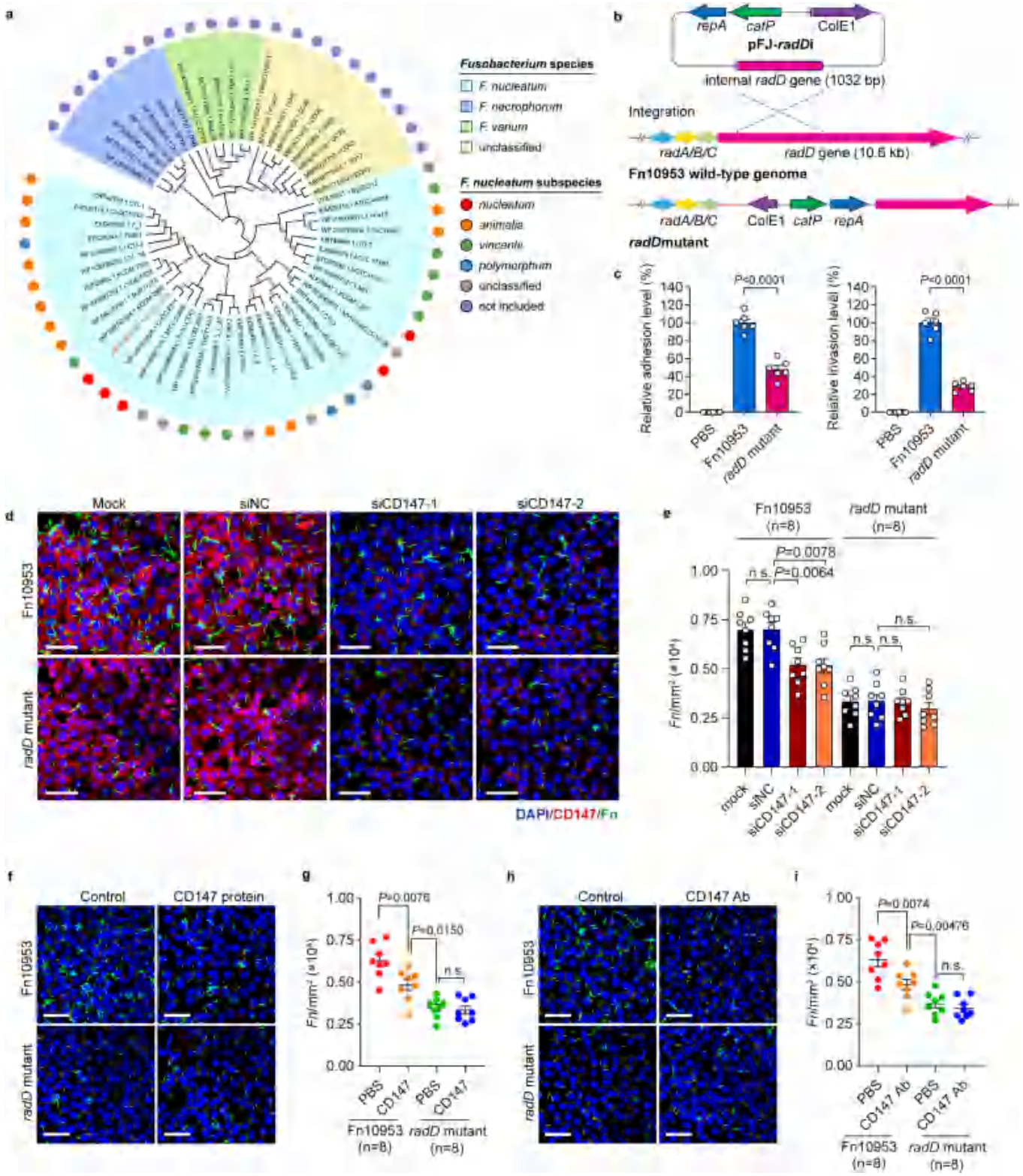


**Extended Data Fig. 7 | See next page for caption.**

https://doi.org/10.1038/s41564-024-01784-w

**Extended Data Fig. 7 | Validate the interaction between RadD and CD147 using the strain *F. nucleatum* ATCC 10953. a**, Phylogenetic analysis of RadD. The maximum-likelihood phylogenetic tree was constructed based on the protein sequences of putative RadD found in Fusobacteria. Light purple circles on branches indicate bootstrap values greater than 0.7 from 300 bootstrap replicates. The sequence of RadD in *F. nucleatum* ATCC 23726 was used as the query (highlighted in red). **b**, Schematic for the generation of *radD* mutant in *F. nucleatum* ATCC 10953 by homologous recombination. **c**, The relative adhesion and invasion level of Fn10953 and *radD* mutant to HCT116 cells (n = 6 biological replicates). **d**, Immunofluorescence analysis of FITC-labeled Fn10953 and *radD* mutant attachment to CD147-depleted (siCD147-1 and siCD147-2) or control (siNC) HCT116 cells. Scale bars, 50 μm. **e**, Quantitation of *F. nucleatum* binding performed in **d** (n = 8 biological replicates). **f** and **g**, Representative images (**f**) and quantitation (**g**) of FITC-labeled (green) Fn10953 and *radD* mutant attachment to DAPI-stained (blue) HCT116 cells preincubated with soluble CD147 proteins (n = 8 biological replicates). Scale bars, 50 μm. **h** and **i**, Representative images (**h**) and quantitation (**i**) of FITC-labeled (green) Fn10953 and *radD* mutant attachment to DAPI-stained (blue) HCT116 cells preincubated with anti-CD147 antibodies (n = 8 biological replicates). Scale bars, 50 μm. Data are presented as mean ± SEM from three independent experiments. *P* values were determined by unpaired two-tailed Student's *t*-test (**c**) and one-way ANOVA with Dunnett's test (**e**) and Turkey's test (**g** and **i**).

https://doi.org/10.1038/s41564-024-01784-w

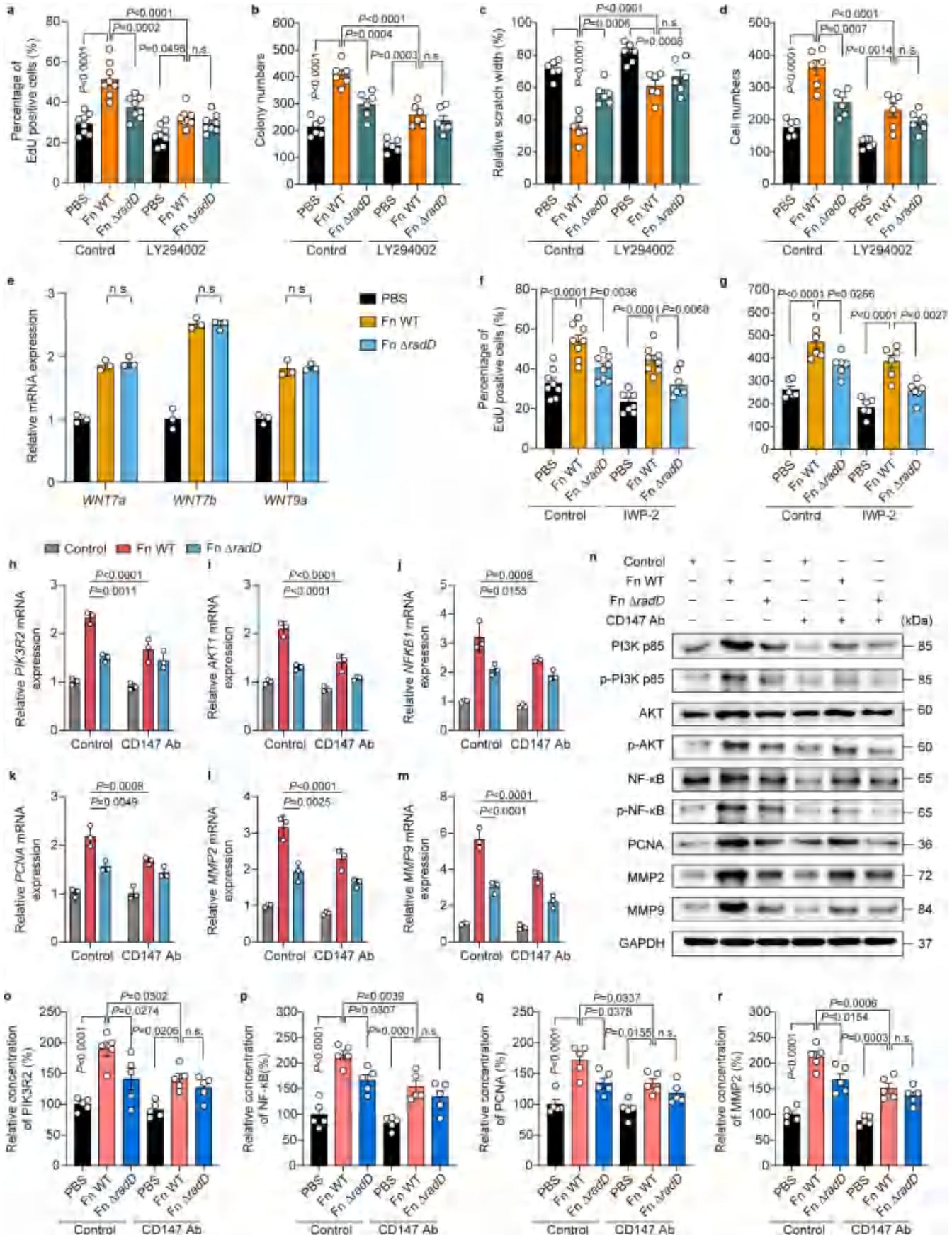


**Extended Data Fig. 8 | See next page for caption.**

https://doi.org/10.1038/s41564-024-01784-w

**Extended Data Fig. 8 | *F. nucleatum* RadD activated CD147-PI3K/AKT/NF-κB pathway in CRC cells. a**–**d**, The pro-tumorigenesis effect mediated by RadD was inhibited when treated with PI3K inhibitor LY294002. Quantitative analysis of the percentages of EdU-positive HCT116 cells (**a**) (n = 8 biological replicates), colony-forming efficiency assay (**b**) (n = 6 biological replicates), scratch assays (**c**) (n = 6 biological replicates) and transwell assays (**d**) (n = 6 biological replicates) of HCT116 cells are shown. **e**, qRT-PCR confirmed that RadD did not affect the expression level of Wnt signaling genes 7a, 7b, and 9a in HCT116 cells (n = 3 biological replicates). **f** and **g**, Fn WT still significantly promoted cell proliferation compared to Fn Δ*radD*, even after the FadA-associated Wnt/β-catenin signaling pathway was suppressed by the Wnt inhibitor IWP-2. Quantitative analysis of the percentages of EdU-positive HCT116 cells (**f**) (n = 8 biological replicates), colony-forming efficiency assay (**g**) (n = 6 biological replicates). **h**–**n**, RT-qPCR (**h**–**m**) and western blot (**n**) was performed in SW480 cells to validate CD147-PI3K-AKT-NF-κB signaling pathway was activated by *F. nucleatum* RadD. The effects of RadD were attenuated by preincubated with anti-CD147 antibodies. n = 3 biological replicates in each group. These blots were from different membranes, each including loading controls, and that a representative loading control is shown here, all uncropped images for all blots are provided as source data. **o**–**r**, The relative concentration of PIK3R2, NF-κB, PCNA and MMP2 were detected using the enzyme-linked immunosorbent assay (n = 5 biological replicates). Data are presented as mean ± SEM from three independent experiments. *P* values were determined by one-way ANOVA with Turkey's test (**a**–**m** and **o**–**r**).

https://doi.org/10.1038/s41564-024-01784-w

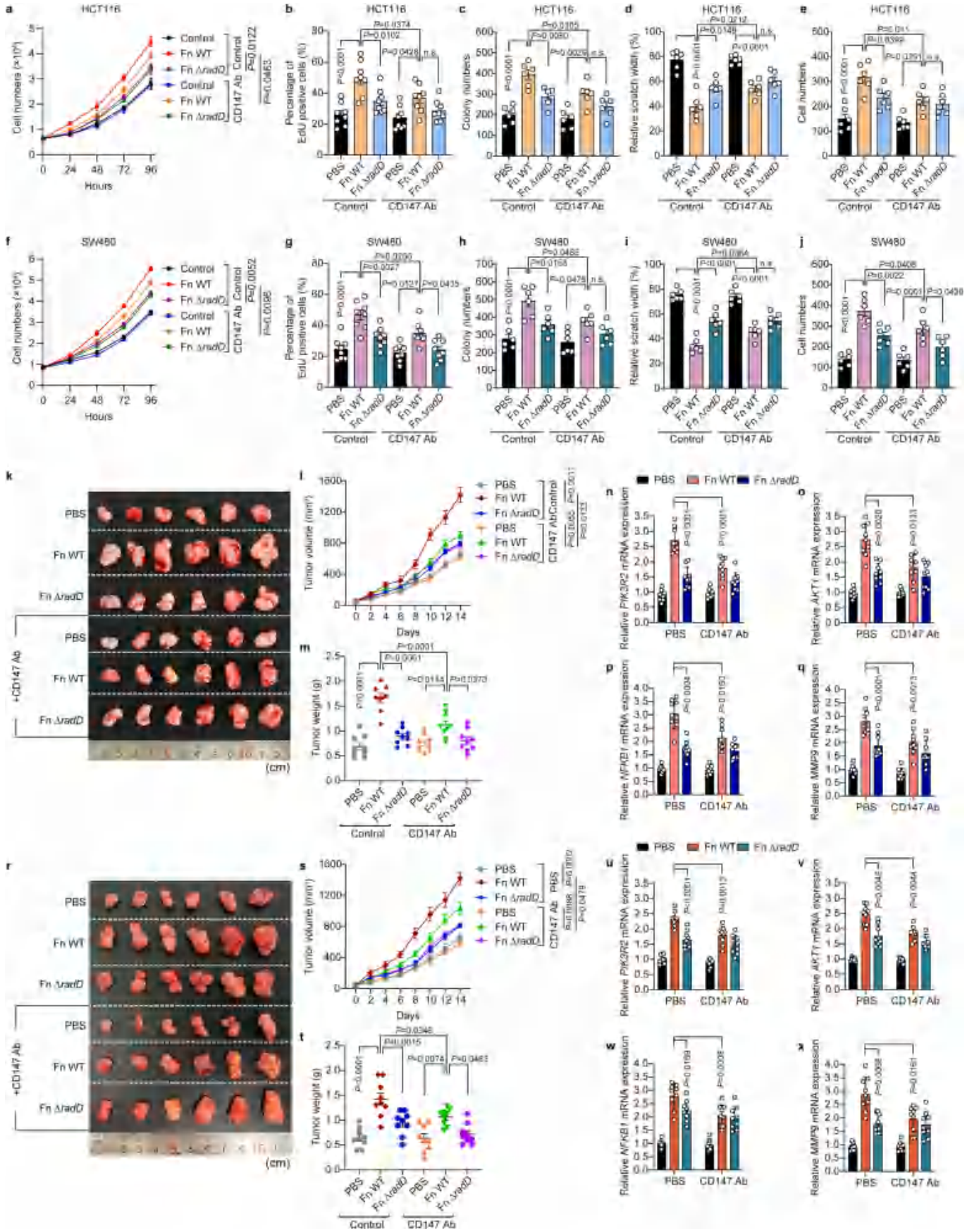


**Extended Data Fig. 9 | See next page for caption.**

https://doi.org/10.1038/s41564-024-01784-w

**Extended Data Fig. 9 | *F. nucleatum* RadD interacted with CD147 to activate the PI3K-AKT pathway and promoted colon tumor growth. a** and **f**, CCK-8 assays were performed to detect the proliferation of HCT116 cells (**a**) or SW480 (**f**) cells after stimulating by Fn WT and Fn Δ*radD* with or without preincubating with anti-CD147 antibodies. PBS was used for negative control. n = 3 biological replicates in each group. **b** and **g**, Quantitation of the percentages of EdU-positive HCT116 cells (**b**) or SW480 cells (**g**) are shown (n = 8 biological replicates). **c** and **h**, Colony-forming efficiency assay of HCT116 cells (**c**) or SW480 cells (**h**) (n = 6 biological replicates). **d** and **i**, Quantitation of HCT116 cells (**d**) and SW480 cells (**i**) migration by scratch assays (n = 6 biological replicates). **e** and **j**, Quantitation of HCT116 cells (**e**) and SW480 cells (**j**) invasion using transwell assays (n = 6 biological replicates). **k**, Representative images of HCT116 subcutaneous tumors. **l** and **m**, The tumor volume ($mm^3$) (**l**) and weight (**g**) (**m**) of BALB/c nude mice bearing HCT116 subcutaneous tumors were measured and shown (n = 9 mice per group). **n**–**q**, RT-qPCR was performed in HCT116 subcutaneous tumor tissues to validate the expression of a subset of key CD147-PI3K–AKT–NF-κB pathway genes (n = 9 biologically independent samples per group). **r**, Images of representative SW480 subcutaneous tumors. **s** and **t**, The tumor volume ($mm^3$) (**s**) and weight (**g**) (**t**) of SW480 subcutaneous tumors were measured and shown (n = 9 mice per group). **u**–**x**, RT-qPCR was performed in SW480 subcutaneous tumor tissues to validate the expression of a subset of key CD147-PI3K–AKT–NF-κB pathway genes (n = 9 biologically independent samples per group). Data are presented as mean ± SEM. *P* values were determined by two-way ANOVA with Turkey's test (**a**, **f**, **l** and **s**), one-way ANOVA with Turkey's test (**b**–**e**, **g**–**j**, **m**–**n**,**q**-**u** and **w**), Brown–Forsythe and Welch ANOVA test with Dunnett's test (**o**-**p**, **v** and **x**).

https://doi.org/10.1038/s41564-024-01784-w

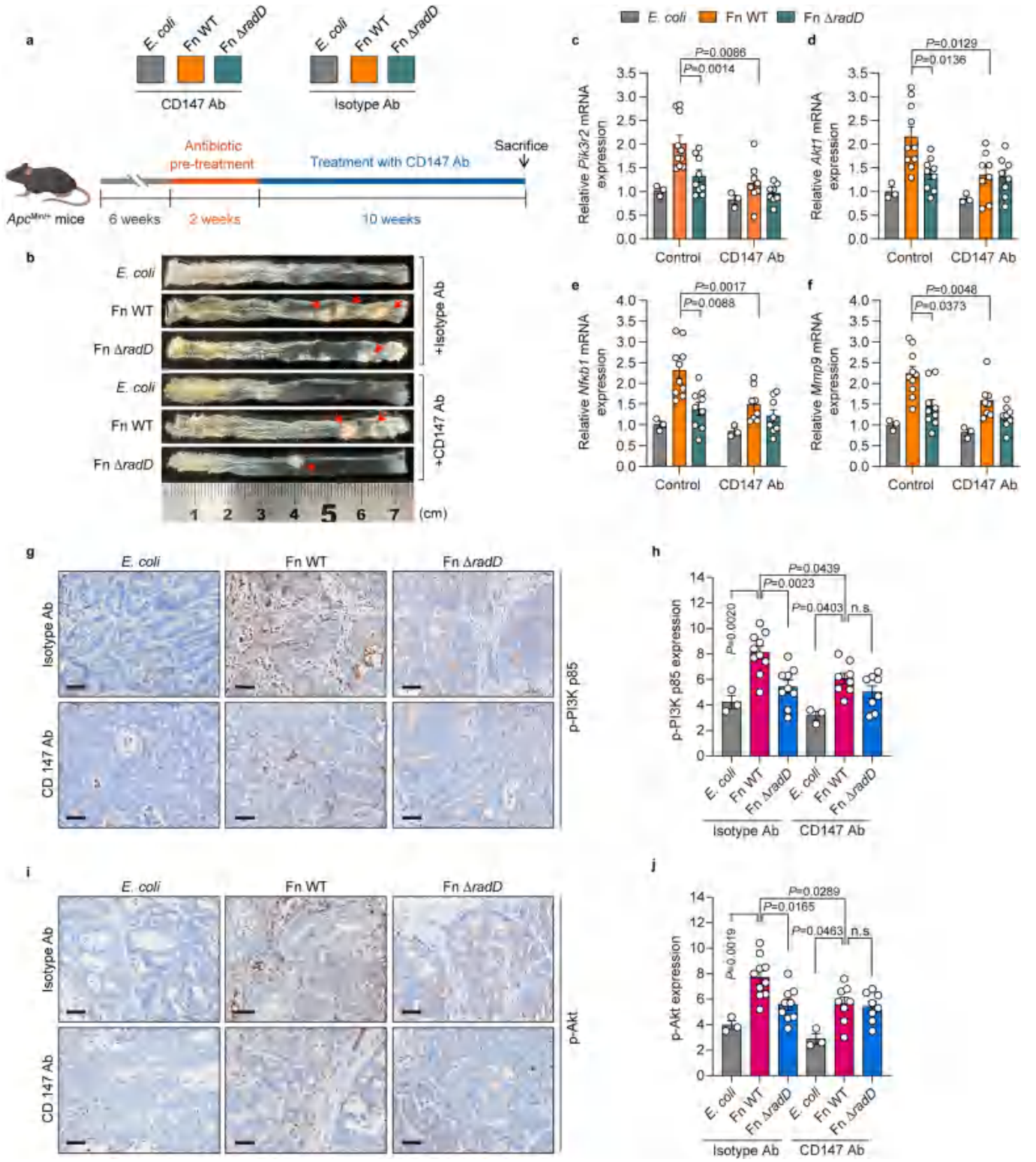


**Extended Data Fig. 10 | Blockade RadD-CD147 interaction reduced the *F. nucleatum*-induced tumor burden in *Apc*$^{Min/+}$ mice. a**, Schematic diagram shows the experimental design of the *Apc*$^{Min/+}$ mouse model. **b**, Representative colonic morphologies of *Apc*$^{Min/+}$ mice from different treatment groups (n = 10 mice per group). **c**–**f**, RT-qPCR was performed in tumor tissues to validate the expression of a subset of key CD147-PI3K–Akt–NF-κB pathway genes. **g** and **i**, Representative immunohistochemistry of p-PI3K (**g**) and p-Akt (**i**) in *Apc*$^{Min/+}$ mice. Scale bars, 50 μm. **h** and **j**, Statistical analysis of immunohistochemical IRS scores of p-PI3K (**h**) and p-Akt (**j**) proteins. Data are presented as mean ± SEM. *P* values were determined by one-way ANOVA with Turkey's test (**c**–**f, h** and **j**). Scheme in panel **a** was partially created with BioRender.com.

nature portfolio

Corresponding author(s): Jing-Yuan Fang

Last updated by author(s): Jun 12, 2024

# Reporting Summary

Nature Portfolio wishes to improve the reproducibility of the work that we publish. This form provides structure for consistency and transparency in reporting. For further information on Nature Portfolio policies, see our Editorial Policies and the Editorial Policy Checklist.

## Statistics

For all statistical analyses, confirm that the following items are present in the figure legend, table legend, main text, or Methods section.

| n/a | Confirmed | |
|---|---|---|
| ☐ | ☒ | The exact sample size (*n*) for each experimental group/condition, given as a discrete number and unit of measurement |
| ☐ | ☒ | A statement on whether measurements were taken from distinct samples or whether the same sample was measured repeatedly |
| ☐ | ☒ | The statistical test(s) used AND whether they are one- or two-sided<br>*Only common tests should be described solely by name; describe more complex techniques in the Methods section.* |
| ☐ | ☒ | A description of all covariates tested |
| ☐ | ☒ | A description of any assumptions or corrections, such as tests of normality and adjustment for multiple comparisons |
| ☐ | ☒ | A full description of the statistical parameters including central tendency (e.g. means) or other basic estimates (e.g. regression coefficient) AND variation (e.g. standard deviation) or associated estimates of uncertainty (e.g. confidence intervals) |
| ☐ | ☒ | For null hypothesis testing, the test statistic (e.g. *F*, *t*, *r*) with confidence intervals, effect sizes, degrees of freedom and *P* value noted<br>*Give P values as exact values whenever suitable.* |
| ☒ | ☐ | For Bayesian analysis, information on the choice of priors and Markov chain Monte Carlo settings |
| ☒ | ☐ | For hierarchical and complex designs, identification of the appropriate level for tests and full reporting of outcomes |
| ☐ | ☒ | Estimates of effect sizes (e.g. Cohen's *d*, Pearson's *r*), indicating how they were calculated |

*Our web collection on statistics for biologists contains articles on many of the points above.*

## Software and code

Policy information about availability of computer code

| | |
|---|---|
| Data collection | The fluorescence intensity of transposon library was measured by fluorescent microplate reader (FLUOstar Omega)<br>The sequencing of mRNA were achieved using novaseq 6000 (Illumina).<br>Quantitative real-time PCR was performed on the StepOnePlus Real-Time PCR system using StepOne Software (v 2.3) (Applied Biosystems).<br>Gels and western blot were visualized by ChemiDoc Imaging Systems using Image Lab Touch Software (v 2.0.0.27) (Bio-Rad).<br>Confocal assay was examined with LSM 710 microscope (Carl Zeiss) using ZEN 2011 software.<br>BD LSRFortessa with FACSDiva software (v 8.0.1) software was used to collect flow cytometry data.<br>Bacterial adhesion or invasion was visualized using Hitachi HT7700 transmission electron microscope. |
| Data analysis | For FACS assay, the fluorescence intensity was analyzed by FlowJo software (v 10.4).<br>Band intensities of western blots were analyzed using ImageJ software (v 1.53).<br>The alignment of RadD homologs was performed using Clustal W software (v 2.1).<br>The maximum-likelihood phylogenetic tree was generated by using MEGA 11 software (v 11.0.11).<br>Statistical analyses were carried out using GraphPad Prism (v 9.4.1). |

For manuscripts utilizing custom algorithms or software that are central to the research but not yet described in published literature, software must be made available to editors and reviewers. We strongly encourage code deposition in a community repository (e.g. GitHub). See the Nature Portfolio guidelines for submitting code & software for further information.

## Data

Policy information about availability of data

All manuscripts must include a data availability statement. This statement should provide the following information, where applicable:

- Accession codes, unique identifiers, or web links for publicly available datasets
- A description of any restrictions on data availability
- For clinical datasets or third party data, please ensure that the statement adheres to our policy

The fecal metagenomic information for the United States and China studies are accessible from the European Nucleotide Archive (ENA; https://www.ebi.ac.uk/ena) with the identifiers PRJEB12449 and PRJEB10878, respectively. For the Japan study, the metadata is available from the DNA Data Bank of Japan database (DDBJ; https://www.ddbj.nij.ac.jp), identified as DRA006684.
RNA-sequencing data have been deposited in the Gene Expression Omnibus (GEO, https://www.ncbi.nlm.nih.gov/geo/) of NCBI and are accessible through the GEO Series accession number GSE245617.Mass spectrometry data have been deposited in the Proteomics Identifications (PRIDE; https://www.ebi.ac.uk/pride/) database under the following accession numbers: PXD053279.

## Research involving human participants, their data, or biological material

Policy information about studies with human participants or human data. See also policy information about sex, gender (identity/presentation), and sexual orientation and race, ethnicity and racism.

| | |
|---|---|
| Reporting on sex and gender | Data were displayed based on self-reporting gender. |
| Reporting on race, ethnicity, or other socially relevant groupings | Race and ethnicity were not considered when designing this study. All patients with colorectal cancer were eligible for analysis without regard to any social grouping. |
| Population characteristics | Population characteristics were all reported in the Supplementary Table 2 and Supplementary Data 2 and 3. These include age, gender and multiple clinical indicators that reflect the severity of colorectal cancer (including tumor size, TNM, AJCC and Ki67). |
| Recruitment | We recruited individuals diagnosed with CRC and scheduled for surgical resection at the Department of Gastrointestinal Surgery between 2015-2020. Cohort 1 were collected from the Western Campus of Renji Hospital, and Cohort 2 and Cohort 3 were collected from the Eastern Campus of Renji Hospital. Patients without follow-up in the next 3 years in our hospital or with unavailable pathological information were excluded from our cohorts; therefore, this may be a potential source of bias. All patients included were from our single medical center and were all Han Chinese; therefore, the results may not apply to every population. Tissues samples were collected from patients whose informed consent was obtained. There was no self-selection or artificial exclusion as patients were enrolled consecutively. There was no patient compensation for participation in this study. |
| Ethics oversight | Renji Hospital Ethics Committee, Shanghai Jiao Tong University School of Medicine, approved the protocol for the study (KY2022-203-B). The patients' written informed consent, including consent to publish indirect identifiers (age, sex and diagnosis), was obtained from all participants. The research was undertaken in compliance with the provisions of the Helsinki Declaration of 1975 and its later amendments. |

Note that full information on the approval of the study protocol must also be provided in the manuscript.

# Field-specific reporting

Please select the one below that is the best fit for your research. If you are not sure, read the appropriate sections before making your selection.

☒ Life sciences ☐ Behavioural & social sciences ☐ Ecological, evolutionary & environmental sciences

For a reference copy of the document with all sections, see nature.com/documents/nr-reporting-summary-flat.pdf

# Life sciences study design

All studies must disclose on these points even when the disclosure is negative.

| | |
|---|---|
| Sample size | No statistical methods were used to predetermine sample size. We used at least 9 mice per group for tumor macroscopic assessment and at least 3 samples for vitro studies, which was sufficient to detect meaningful differences based on previous similar experiments and published literatures (PMID: 31501538, 37069401) |
| Data exclusions | For in vivo experiments and in vitro studies, no data was excluded. |
| Replication | All experiments were repeated three times as three independent experiments , and they yielded comparable results. |
| Randomization | For in vivo experiments, animals were randomly assigned to experimental groups using a randomization chart. For in vitro experiments, randomization was not used due to cell homogeneity and covariates were controlled by seeding all groups at the same cell densities and |

| | |
|---|---|
| | maintaining them in the same growth and media conditions except the intervention. Furthermore, different intervention groups were handled simultaneously whenever possible. |
| Blinding | No blinding was used in the study because groups were given different treatments and analysis was performed by the same investigators, so blinding was not possible. |

# Reporting for specific materials, systems and methods

We require information from authors about some types of materials, experimental systems and methods used in many studies. Here, indicate whether each material, system or method listed is relevant to your study. If you are not sure if a list item applies to your research, read the appropriate section before selecting a response.

## Materials & experimental systems

| n/a | Involved in the study |
|---|---|
| ☐ | ☒ Antibodies |
| ☐ | ☒ Eukaryotic cell lines |
| ☒ | ☐ Palaeontology and archaeology |
| ☐ | ☒ Animals and other organisms |
| ☒ | ☐ Clinical data |
| ☒ | ☐ Dual use research of concern |
| ☒ | ☐ Plants |

## Methods

| n/a | Involved in the study |
|---|---|
| ☒ | ☐ ChIP-seq |
| ☐ | ☒ Flow cytometry |
| ☒ | ☐ MRI-based neuroimaging |

## Antibodies

| | |
|---|---|
| Antibodies used | Anti-RadD antibody was generated by ABclonal Inc., 1:5000 dilution<br>Anti-human CD147 antibody (Abcam, Cat#ab230921), 1:1000 dilution<br>Anti-mouse CD147 antibody (eBioscience, Cat#16-1471-025), 50 μg per mouse<br>Rat IgG2a isotype control (eBioscience, Cat#14-4321-85), 50 μg per mouse<br>Anti-PI3Kp85 antibody (ABclonal, Cat#A4860), 1:500 dilution<br>Anti-PI3Kp85/p55 (Y467/Y199) antibody (ABclonal, Cat#AP0854), 1:1000 dilution<br>Anti-AKT1 antibody (ABclonal, Cat#A17909), 1:2000 dilution<br>Anti-phospho-AKT1 (S473) antibody (ABclonal, Cat#AP0637), 1:1000 dilution<br>Anti-MMP2 antibody (ABclonal, Cat#A19080), 1:1000 dilution<br>Anti-MMP9 antibody (ABclonal, Cat#A0289), 1:500 dilution<br>Anti GAPDH antibody (ABclonal, Cat#AC033), 1:10000 dilution<br>Anti-Ki67 antibody (Cell Signaling Technology, Cat#12202S), 1:500 dilution<br>Anti-NF-κB p65 antibody (Cell Signaling Technology, Cat#8242S), 1:1000 dilution<br>Anti-phospho NF-κB p65 (S536) antibody (Cell Signaling Technology, Cat#3033S), 1:1000 dilution<br>Anti-PCNA antibody (Cell Signaling Technology, Cat#2586S), 1:1000 dilution<br>Goat anti-mouse IgG(H+L) secondary antibody, Alexa Fluor 594 (Cell Signaling Technology, Cat#8890S), 1:500 dilution |
| Validation | The validation information or related references can be obtained within the following links:<br>1. Anti-RadD antibody was produced by ABclonal Inc. according to a published protocol (PMID: 34074747). Briefly, the recombinant protein RadD41-360 (residues 41-360) was purified and used as the antigen, and the serum with a high titer and specificity was obtained from immunized rabbit.<br>2. Anti-human CD147 antibody (Abcam, Cat#ab230921)<br>https://www.abcam.cn/products/primary-antibodies/cd147-antibody-10e10-ab230921.html<br>3. Anti-mouse CD147 antibody (eBioscience, Cat#16-1471-025)<br>https://www.thermofisher.com/antibody/product/CD147-Antibody-clone-RL73-Monoclonal/16-1471-025<br>4. Rat IgG2a isotype control (eBioscience, Cat#14-4321-85)<br>https://www.thermofisher.com/antibody/product/Rat-IgG2a-kappa-clone-eBR2a-Isotype-Control/14-4321-85<br>5. Anti-PI3Kp85 antibody (ABclonal, Cat#A4860)<br>https://abclonal.com.cn/catalog/A4860<br>6. Anti-PI3Kp85/p55 (Y467/Y199) antibody (ABclonal, Cat#AP0854)<br>https://abclonal.com.cn/catalog/AP0854<br>7. Anti-AKT1 antibody (ABclonal, Cat#A17909)<br>https://abclonal.com.cn/catalog/A17909<br>8. Anti-phospho-AKT1 (S473) antibody (ABclonal, Cat#AP0637)<br>https://abclonal.com.cn/catalog/AP0637<br>9. Anti-MMP2 antibody (ABclonal, Cat#A19080)<br>https://abclonal.com.cn/catalog/A19080<br>10. Anti-MMP9 antibody (ABclonal, Cat#A0289)<br>https://abclonal.com.cn/catalog/A0289<br>11. Anti GAPDH antibody (ABclonal, Cat#AC033)<br>https://abclonal.com.cn/catalog/AC033<br>12. Anti-Ki67 antibody (Cell Signaling Technology, Cat#12202S)<br>https://www.cellsignal.cn/products/primary-antibodies/ki-67-d3b5-rabbit-mab-ihc-formulated/12202<br>13. Anti-NF-κB p65 antibody (Cell Signaling Technology, Cat#8242S)<br>https://www.cellsignal.cn/products/primary-antibodies/nf-kb-p65-d14e12-xp-rabbit-mab/8242 |

14. Anti-phospho NF-κB p65 (S536) antibody (Cell Signaling Technology, Cat#3033S)
https://www.cellsignal.cn/products/primary-antibodies/phospho-nf-kb-p65-ser536-93h1-rabbit-mab/3033
15. Anti-PCNA antibody (Cell Signaling Technology, Cat#2586S)
https://www.cellsignal.cn/products/primary-antibodies/pcna-pc10-mouse-mab/2586
16. Goat anti-mouse IgG(H+L) secondary antibody, Alexa Fluor 594 (Cell Signaling Technology, Cat#8890S)
https://www.cellsignal.cn/products/secondary-antibodies/anti-mouse-igg-h-l-f-ab-2-fragment-alexa-fluor-594-conjugate/8890

## Eukaryotic cell lines

Policy information about cell lines and Sex and Gender in Research

| | |
|---|---|
| Cell line source(s) | HCT116 (ATCC, Cat#CCL-247), SW480 (ATCC, Cat#CCL-228), RKO (ATCC, Cat#CRL-2577), DLD1 (ATCC, Cat#CCL-221), HT29 (ATCC, Cat#HTB-38), Caco2 (ATCC, Cat#HTB-37), CT26 (ATCC, CRL-2638), MC38 (BMCR, Cat#1101MOU-PUMC000523) |
| Authentication | STR examied |
| Mycoplasma contamination | Routine mycoplasma testing was negative. |
| Commonly misidentified lines (See ICLAC register) | No commonly misidentified cell lines were used in the study. |

## Animals and other research organisms

Policy information about studies involving animals; ARRIVE guidelines recommended for reporting animal research, and Sex and Gender in Research

| | |
|---|---|
| Laboratory animals | BALB/c nude mice were purchased from Shanghai Model Organisms (Shanghai, China). ApcMin/+ mice were obtained from Jackson Laboratory (Bar Barbor, ME, USA). Mice were housed (no more than five per cage) in a specific pathogen-free animal facility at 20-26 degree Celsius, 40%-70% humidity under a 12-h light/12-h dark photoperiod, with free access to food and water. |
| Wild animals | No wild animals were used in the study. |
| Reporting on sex | Findings from our study only applied to male mice. |
| Field-collected samples | No field collected samples were used in the study. |
| Ethics oversight | All animal procedures were conducted in compliance with the guidelines of the Shanghai Model Organisms Center, Institutional Animal Care and Use Committee (SMOC IACUC). |

Note that full information on the approval of the study protocol must also be provided in the manuscript.

## Plants

| | |
|---|---|
| Seed stocks | NA |
| Novel plant genotypes | NA |
| Authentication | NA |

## Flow Cytometry

### Plots

Confirm that:

☒ The axis labels state the marker and fluorochrome used (e.g. CD4-FITC).

☒ The axis scales are clearly visible. Include numbers along axes only for bottom left plot of group (a 'group' is an analysis of identical markers).

☒ All plots are contour plots with outliers or pseudocolor plots.

☒ A numerical value for number of cells or percentage (with statistics) is provided.

## Methodology

| | |
|---|---|
| Sample preparation | Bacteria were grown overnight, washed twice in sterile PBS, and then labeled with FITC (0.1 mg/mL in PBS, Yeasen Biotechnology, Shanghai, China) for 2 h at 37 degree Celsius. After three additional washes with PBS, FITC-labeled bacteria were used at an MOI of 50. Bacteria were incubated with cells in 12-well plates for 1 h in an incubator at 37 degree Celsius. Post-incubation, the cells were subjected to two PBS washes, followed by cell recovery in preparation for flow cytometry. |
| Instrument | BD LSRFortessa |
| Software | Samples were collected by FACSDiva (v 8.0.1) software and analyzed using FlowJo software (v 10.4). |
| Cell population abundance | Minimum 10,000 events collected for analysis. |
| Gating strategy | Forward scatter (FSC) and side scatter (SSC) strategies were used for gating followed by an elimination of the doublets based on the size scatter. The isotype control samples were used to define background. |

☒ Tick this box to confirm that a figure exemplifying the gating strategy is provided in the Supplementary Information.